

Flavour and Electroweak Precision Constraints on a Simplified Dark Matter Model with a Light Spin-0 Mediator

Lipika Kolay,^a Soumitra Nandi.^a

^a*Department of Physics, Indian Institute of Technology Guwahati,
North Guwahati, Assam-781039, India,*

E-mail: klipika@iitg.ac.in, soumitra.nandi@iitg.ac.in

ABSTRACT: This work investigates the allowed parameter spaces of a simplified dark matter (DM) model characterized by a spin-0 mediator with masses in the low to intermediate range (< 10 GeV). We systematically divide the parameter space into various mass regions of the mediator and constrain the model parameters using a diverse set of observables, including flavour-changing charged and neutral current processes such as rare and semi-leptonic decays of pseudoscalar mesons (B and K), electroweak precision observables alongside data from fixed-target experiments. Additionally, we explore the model's capability to explain recent Belle-II data on invisible B-meson decays. Our study includes a detailed examination of DM properties and the constraints from Big Bang nucleosynthesis. We present bounds on model parameters through individual and simultaneous analyses of the available inputs and highlight their implications for understanding DM phenomenology. Furthermore, we obtain the bound on the couplings of the possible gauge invariant dimension-5 operators, leading to the possible interactions between the spin-0 mediator and the SM gauge bosons and fermions. This study comprehensively investigates the constraints and theoretical implications associated with low-mass spin-0 mediator DM models.

KEYWORDS: Simplified Models, Dark Matter, Flavour observables, EWPOs

Contents

1	Introduction	2
2	Working Model: Simplified Dark Matter	3
3	Theory Framework	5
3.1	FCCC and FCNC effective Vertices	5
3.1.1	FCNC Processes	6
3.1.2	FCCC Observables	6
4	Implications for Various Observables	7
4.1	Observables Related to FCNC Processes	7
4.1.1	Neutral Meson Mixing	7
4.1.2	Rare Decays of Mesons	10
4.1.3	Fix Target Experiment	11
4.1.4	Invisible Decays of Mesons	12
4.2	FCCC Observables	17
4.3	Electroweak Precision Observables	18
4.4	Cosmological Constraints	19
4.5	DM Constraints	20
5	Analysis and Results	23
5.1	Constraints from Flavour and Electroweak Precision Observables	23
5.1.1	Bounds from Fixed Target Experiment	24
5.1.2	Bounds from Semileptonic $B(B_s) \rightarrow K^{(*)}(\phi) \ell^+ \ell^-$ Decays	24
5.1.3	Allowed Parameter Spaces from the Data on Flavour and EWPOs	26
5.2	Cosmological Constraints	30
5.3	Combined analysis: Flavour + EWPOs + DM	31
6	Other Important Bounds	34
6.1	Bounds on Dimensionless Couplings	34
6.2	Bounds on a Toy Model Parameters	35
7	Summary	36
A	DM-electron cross-section	37
B	Allowed parameter spaces from the data on dark sector	38

1 Introduction

The Standard Model (SM) of particle physics is successful in describing many phenomena of nature at the fundamental level, however, the model falls short in explaining certain key aspects of nature. It lacks a viable candidate for dark matter (DM) and struggles to accommodate observed baryon asymmetry. Furthermore, the model does not provide a mechanism for neutrino mass generation. To address these deficiencies, various extensions of the SM have been proposed. All these extensions introduce new degrees of freedom and interactions at higher energy scales and provide suitable DM candidates to explain the observed pattern in the data on DM searches and baryon asymmetry. The low-energy observables could play a crucial role in probing the new interactions beyond the SM (BSM), in such cases, we need to look for deviations between the measured and the predicted values (SM) of the relevant observables. In experimental searches for DM, it is convenient to study the signatures of this DM candidate in a model-independent way using an effective field theory (EFT) approach. This approach involves identifying interactions between DM particles and SM fields through a set of non-renormalizable operators, characterized by an effective scale Λ and the DM mass. However, given the limitations of the applicability of the DM EFT at the center-of-mass energies at the LHC, the recent searches at the ATLAS and CMS rely on the simplified DM models (SDM); for the details, see the analyses of the refs. [1–19]. Among the various possibilities of the NP particles, the LHCb and ATLAS are continuously searching for scalar and pseudoscalar mediators [20–26] which is our main focus in this study. Furthermore, pseudoscalar mediators have gained a lot of attention in explaining indirect detection bounds.

The phenomenology of low-mass DM interacting with the SM through scalar and pseudoscalar mediators has been explored in literature [27–34]. A few studies of simplified models, involving either scalar or pseudoscalar mediators, focus on some flavour-changing neutral current (FCNC) processes such as $B_{(s)} \rightarrow \mu\mu$, $B \rightarrow K + X$, and $K \rightarrow \pi + X$ [28, 32]. These flavour observables being suppressed in the SM provide a unique framework to constrain the interactions between the SM and dark sector particles. The coupling structure of these interactions can vary from being flavour universal [28, 29] to non-universal [13, 32]. Additionally, studies on dark sector phenomena, such as DM relic density and direct detection (DD) constraints, provide valuable insights into the mediator’s connection with DM and its interaction strength with the SM [27, 28, 32–34]. Pseudoscalar mediator models are particularly exciting because they most notably address indirect detection constraints by accommodating the long-standing DAMA [35] modulated signal and by explaining the 1–3 GeV gamma-ray excess at the Galactic Center [36] while maintaining the correct relic density today [29, 32]

Flavour physics might be important in indirectly detecting new particles or interactions beyond the SM. In this regard, semi-leptonic rare B and K decays may serve as a particularly valuable tool. These decays offer relatively clean experimental signatures, manageable theoretical uncertainties, and suppressed rates in the SM, making them sensitive probes of BSM physics. Observables related to the neutral-current transition $b \rightarrow s\mu^+\mu^-$, such as the branching ratios and the angular observables in $B \rightarrow K^{(*)}\mu^+\mu^-$ decays have been measured

by LHCb [37–40] and Belle collaboration [41]. The measured value of angular observable like P'_5 are not in complete agreement with its SM prediction [42–44]. Furthermore, the measurement of the branching fraction of the rare $B_s \rightarrow \mu^+\mu^-$ decay is also available [45], which plays an important role in constraining the NP parameter spaces.

Recently, the Belle-II collaboration reported an analysis of the rare FCNC process $B^+ \rightarrow K^+\nu\bar{\nu}$ [46], the measured value of the branching fraction shows an excess of 2.7σ above the SM prediction [47]. Similar to this decay, there are other FCNC invisible decays, like $B^0 \rightarrow K^{(*)}\nu\bar{\nu}$, $K_{L,S} \rightarrow \pi\nu\bar{\nu}$, $B \rightarrow \rho\nu\bar{\nu}$, and $B \rightarrow \phi\nu\bar{\nu}$, for which the upper bounds on the respective branching fractions are available [46, 48–52]. In these searches, neutrinos go undetected, and their possible signature is traced via missing energy signals. As we know, the missing energy signals are the revelatory clue of the production of stable neutral particles. Like neutrinos, any other invisible particles will also go undetected and could produce missing energy signals. One of the most common examples of such a neutral particle beyond the SM is the DM. It is to be noted that non-standard interactions of neutrinos may also contribute to the above rare decays or to any other missing energy signal. However, this work will consider the missing energy signals via the DM in the final state of the rare decays mentioned above. We will consider SDM with spin-0 mediator S and the fermionic DM χ . Therefore, depending on the kinematics (masses of the DM and the mediator), the additional contributions from the SDM to the rare FCNC processes will be either via the three body $d_i \rightarrow d_j\chi\bar{\chi}$ ($d_{i/j}$ down type quarks) transitions or via the two body $d_i \rightarrow d_jS$ decays, with S an undetected particle. Inputs are available for the branching ratios of the decays $K_L^{(+)} \rightarrow \pi^{0(+)}S$ [51, 53] and for $B \rightarrow KS$ [54].

Apart from the flavour data, electroweak precision observables (EWPOs) play a crucial role in testing the allowed parameter spaces. These observables include measurements related to the properties of the W and Z bosons, such as their masses and decay rates, as well as other precision electroweak parameters.

This paper is organised as follows: in Sec. 2 and Sec. 3, we discuss the particle content and possible interactions of the simplified model we have considered and the methodology used to calculate the loop contributions. Sec. 4 describes the impact of the NP on various observables including flavour changing charge current (FCCC), FCNC, and EWPOs along with cosmological constraints. Finally, in Sec. 5, we discuss and analyse our results for all observables, both separately and simultaneously with DM and other constraints. The bounds on a toy model are discussed in Sec. 6. We conclude by summarising our findings in Sec. 7.

2 Working Model: Simplified Dark Matter

We have considered an extension of the SM by a singlet Dirac fermion dark matter χ , which is odd under the discrete symmetry \mathbb{Z}_2 ($\chi \rightarrow -\chi$). The spin-0 singlet S is communicating with SM as well as the DM. The relevant Lagrangian can be written as [8, 33, 55, 56] :

$$\mathcal{L} = \mathcal{L}_{SM} + \frac{1}{2}\bar{\chi}(i\not{\partial} - m_\chi)\chi + \frac{1}{2}\partial_\mu S\partial^\mu S - \mathcal{L}_{\bar{\chi}\chi S} - \mathcal{L}_{\bar{\psi}\psi S} - \mathcal{L}_{VVS} - V(S, H). \quad (2.1)$$

The interactions of S with the DM (χ) and the SM fermions (ψ) are written as

$$\begin{aligned}\mathcal{L}_{\bar{\chi}\chi S} &= \bar{\chi}(c_{s\chi} + ic_{p\chi}\gamma_5)\chi S, \\ \mathcal{L}_{\bar{\psi}\psi S} &= m_\psi\bar{\psi}(c_s + ic_p\gamma_5)\psi S.\end{aligned}\tag{2.2}$$

with, $c_s = \frac{\sqrt{2}g_s}{v}$, $c_p = \frac{\sqrt{2}g_p}{v}$, v being the vacuum expectation value (VEV) of SM Higgs and $g_{s(p)}$ are dimensionless couplings. Here, the $S\bar{\psi}\psi$ couplings satisfy the criterion of Minimal Flavour Violation (MFV) and we could avoid any contributions to the FCNC processes at the tree level. The interactions of the spin-0 boson S with the SM gauge bosons are defined by

$$\mathcal{L}_{VVS} = c'_W W_\mu^+ W^{\mu-} S + c'_Z Z_\mu Z^\mu S.\tag{2.3}$$

Here, the gauge bosons-mediator couplings is written as

$$c'_V = 2M_V^2 c_G,\tag{2.4}$$

with $c_G = \frac{g_V}{v}$, so that the NP couplings will be in the same scale as the previous $S\bar{f}f$ couplings. The scalar potential $V(S, H)$ is defined as

$$V(S, H) = \frac{\mu_S^2}{2}S^2 + \frac{\lambda_3}{3!}S^3 + \frac{\lambda_4}{4!}S^4 + \lambda_1 SH^\dagger H + \lambda_2 S^2 H^\dagger H + \mu_h^2 H^\dagger H + \frac{1}{2}\lambda_H (H^\dagger H)^2.\tag{2.5}$$

Here H is SM Higgs doublet given by: $H = \{0, \frac{(v+h)}{\sqrt{2}}\}$.

In principle, the mediator S could mix with the SM Higgs. However, we have kept those mixing parameters (λ_1) to be small. The similar simplified model is considered in our pervious work [56], where we studied the phenomenology focused on the high-mass region of the mediator i.e $M_S \geq 100$ GeV. In this work, we intend to study the low-mass region of the mediator, i.e., for the region $M_S \leq 10$ GeV. The corresponding possible higher dimensional operators and UV completion of this simplified model are discussed in detail in [56].

The dimension-5 SM gauge invariant operators could lead to the interaction given in eq. (2.2) between the SM fermions and the S are as follows [56]

$$\mathcal{L}_{\text{dim-5}} = \mathcal{L}_{\text{ferm}} + \mathcal{L}_{\text{gauge}},\tag{2.6}$$

with

$$\mathcal{L}_{\text{ferm}} = -\frac{C}{\Lambda}[\bar{\psi}_L i\gamma_5 H \psi_R P] - y_f[\bar{\psi}_L H \psi_R] + h.c.\tag{2.7}$$

and

$$\mathcal{L}_{\text{gauge}} = \frac{C'}{\Lambda}P|D_\mu H|^2.\tag{2.8}$$

Here, the field P is defined as

$$P = u + S_1,\tag{2.9}$$

with u as the VEV associated with the P field. With the given H and P , we expand the above Lagrangian. We note that the mass term of the fermions receives an additional contribution $\propto \gamma_5$. To remove this γ_5 dependent term, we use the following chiral rotation to the fermionic fields

$$\psi \rightarrow e^{\frac{i\gamma_5\alpha}{2}}\psi, \quad \psi_L \rightarrow e^{-\frac{i\alpha}{2}}\psi_L, \quad \psi_R \rightarrow e^{\frac{i\alpha}{2}}\psi_R,\tag{2.10}$$

where

$$\tan \alpha = \frac{Cuv}{y_f \Lambda}. \quad (2.11)$$

Using this procedure, we get the interactions between the fermion fields and the spin-0 scalar as

$$\mathcal{L}_{\text{ferm}} \supset -\mathbb{C}_s^S [\bar{\psi}\psi S] - \mathbb{C}_p^S [\bar{\psi}i\gamma_5\psi S] - \mathbb{C}_s^{h_1} [\bar{\psi}\psi h_1] - \mathbb{C}_p^{h_1} [\bar{\psi}i\gamma_5\psi h_1], \quad (2.12)$$

with

$$\begin{aligned} \mathbb{C}_s^{h_1} &= \left(\frac{y_f}{\sqrt{2}} - \frac{Cu\alpha}{\Lambda\sqrt{2}} \right) \cos \theta + \frac{Cv\alpha}{\Lambda\sqrt{2}} \sin \theta, & \mathbb{C}_p^{h_1} &= \left(\frac{Cu}{\Lambda\sqrt{2}} + \frac{y_f\alpha}{\sqrt{2}} \right) \cos \theta - \frac{Cv}{\Lambda\sqrt{2}} \sin \theta, \\ \mathbb{C}_s^S &= \left(\frac{y_f}{\sqrt{2}} - \frac{Cu\alpha}{\Lambda\sqrt{2}} \right) \sin \theta - \frac{Cv\alpha}{\Lambda\sqrt{2}} \cos \theta & \text{and} & \quad \mathbb{C}_p^S = \left(\frac{Cu}{\Lambda\sqrt{2}} + \frac{y_f\alpha}{\sqrt{2}} \right) \sin \theta - \frac{Cv}{\Lambda\sqrt{2}} \cos \theta. \end{aligned} \quad (2.13)$$

In these equations, the angle θ is defined via the following mixing between S_1 and h

$$\begin{aligned} h_1 &= \cos \theta h - \sin \theta S_1, \\ S &= \sin \theta h + \cos \theta S_1. \end{aligned} \quad (2.14)$$

Here, h_1 and S are the SM scalar and new scalar defined in their mass basis, respectively. In the above equations, we have obtained the fields S and h_1 from a mixing of S_1 and h with the mixing angle θ . For the details, please see the discussion in ref. [56]. We can compare the field S with the new spin-0 scalar and h_1 as the SM Higgs.

Similarly, after expanding the gauge interaction term in eq. (2.8) we obtain

$$\mathcal{L}_{\text{gauge}} = \mathbb{C}_W^S W^{+\mu} W_\mu^- S + \mathbb{C}_Z^S Z_\mu Z^\mu S, \quad (2.15)$$

with

$$\mathbb{C}_W^S = \frac{2M_W^2}{v} \sin \theta + \frac{C'M_W^2}{\Lambda} \cos \theta \quad \text{and} \quad \mathbb{C}_Z^S = \frac{M_Z^2}{v} \sin \theta + \frac{C'M_{Z^2}}{2\Lambda} \cos \theta. \quad (2.16)$$

This is the simplest example of a dimension-5 operator from which we can generate the type of interactions we are interested in. There could be more complex scenarios in which one could generate similar structures, but that is beyond the scope of this paper.

3 Theory Framework

3.1 FCCC and FCNC effective Vertices

In this section, we will focus on the contributions of our model in various FCNC and FCCC vertices. It is well known that FCNC processes are loop-suppressed within the SM, making them particularly sensitive to potential new interactions beyond the SM. In contrast, FCCC processes occur at the tree level in the SM, meaning any contributions from new physics scenarios would be tightly constrained. Given the current level of precision, data from these processes can be instrumental in constraining the parameters of new physics models that contribute at the loop level [56]. The interactions described in eqs. (2.2) and (2.3) do not contribute to FCNC and FCCC processes at the tree level, with effects only arising at the loop level. These new interactions will alter the FCNC and FCCC vertices. We will explore these modifications in the following discussion.

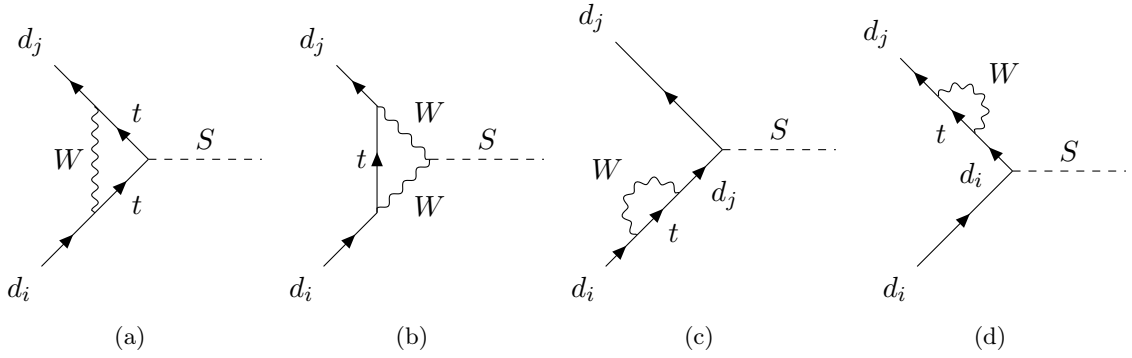


Figure 1. Feynman diagrams depicting the FCNC vertex correction for the $d_i \rightarrow d_j S$ vertex. In these diagrams, all the internal quarks are shown only with the top quark. Similar diagrams with c-quark and u-quark are also possible.

3.1.1 FCNC Processes

In the SDM considered above, the contribution to the FCNC processes will be through the one-loop diagrams shown in Fig. 1 for the $d_i \rightarrow d_j S$ vertex. The contribution from the above diagrams can be expressed as:

$$\mathcal{L}_{eff}^{bsS} = \frac{2\sqrt{2}G_F M_W^2}{16\pi^2} V_{td_i} V_{td_j}^* \left[C_1 [\bar{d}_j (m_{d_j} P_L + m_{d_i} P_R) d_i] + C_2 [\bar{d}_j (m_{d_j} P_L - m_{d_i} P_R) d_i] \right] S, \quad (3.1)$$

where C_1 and C_2 are the effective coefficients coming from the loop diagrams. Now, the loop contributions contain divergences, which is not surprising. The details on this is discussed in ref. [56]. With the leading-log approximation the dominant contributions in C_1 and C_2 from the diagrams in Fig. 1 can be expressed as

$$\begin{aligned} C_1(\Lambda) &= \frac{m_t^2}{2M_W^2} \left((3c_s) \log \frac{\Lambda^2}{m_t^2} + (3c_G) \log \frac{\Lambda^2}{M_W^2} \right), \\ C_2(\Lambda) &= \frac{m_t^2}{2M_W^2} (ic_p) \log \frac{\Lambda^2}{m_t^2}. \end{aligned} \quad (3.2)$$

The detailed calculations of the loops are discussed in [56].

3.1.2 FCCC Observables

We will also have contribution to the FCCC process via one-loop penguin diagram along with the counter-term diagrams. All the relevant diagrams are shown in Fig. 2. The general contribution considering all the loops will be given by the following:

$$\mathcal{L}_{u_i \rightarrow d_j W}^{eff} = \frac{-gV_{ij}^*}{2\sqrt{2}} [C_{VL} \bar{d}_j \gamma_\mu (1 - \gamma_5) u_i + C_{VR} \bar{d}_j \gamma_\mu (1 + \gamma_5) u_i] W^\mu. \quad (3.3)$$

Here, the impact of new physics arising from loop corrections is reflected in the coefficients C_{VL} and C_{VR} . Thus, in the tree-level scenario (purely within the SM), $C_{VL} = 1$ and

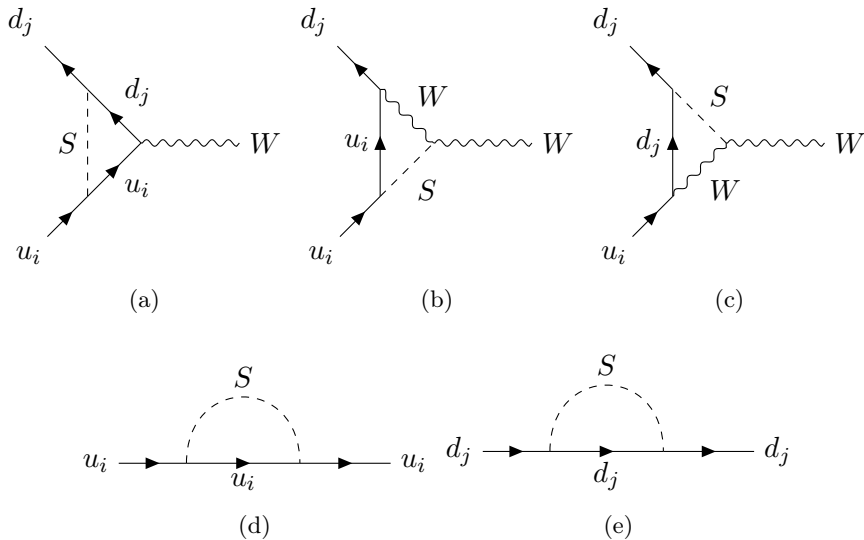


Figure 2. Feynman diagrams contributing as a correction to $u_i \rightarrow d_j W$ vertex and self-energy corrections to the up and down type quark fields which are relevant for the wave function renormalizations.

$C_{VR} = 0$. The expression for C_{VL} and C_{VR} , diagram-wise, can be found in ref. [56]. Hence, the total contributions to C_{VL} and C_{VR} in eq. (3.3) could be written as

$$C_{VL} = C_{VL}^{2b} + C_{VL}^{2c} + C_{VL}^{\text{counter}}, \quad C_{VR} = C_{VR}^{2a} + C_{VR}^{2b} + C_{VR}^{2c}. \quad (3.4)$$

In the following section, we will discuss the various observables potentially sensitive to these $d_i \rightarrow d_j S$ transitions and the new contributions to the FCCC vertices.

4 Implications for Various Observables

This section will examine how our model affects various observables, with new contributions emerging through the 1-loop corrections in FCNC and FCCC vertices discussed earlier. First, we will address observables associated with the FCNC and FCCC processes. Furthermore, we will discuss the impact of our model on the electroweak observables in separate subsections.

4.1 Observables Related to FCNC Processes

4.1.1 Neutral Meson Mixing

The mixing between neutral pseudoscalar mesons is important for constraining NP models since the data here are very precise. In our model, the contribution to the meson mixing amplitude will come from the Feynman diagram shown in Fig. 3a. In the last section, we have shown the $d_i \rightarrow d_j S$ effective vertex calculation. In this study, we focus on the mediator's low mass region, where the mediator's mass ranges are considered in the GeV and sub-GeV regions. For decays like $P \rightarrow P' \ell \ell$, the di-lepton invariant mass square q^2 will be in the range $(2m_\ell)^2 \leq q^2 \leq (M_P - M_{P'})^2$. So, we cannot Taylor expand the S

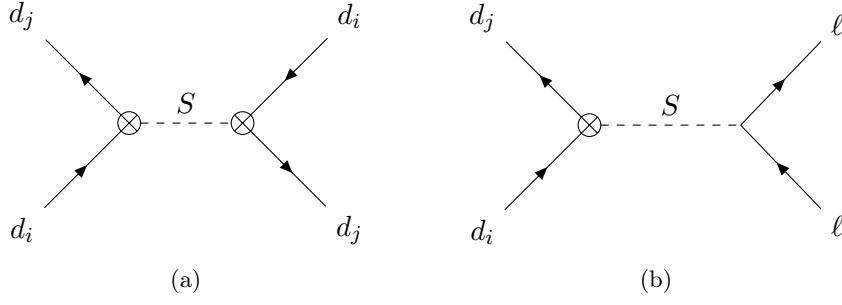


Figure 3. Feynman diagram contributing to the quark level processes of neutral meson mixing and $b \rightarrow s\ell\ell$, $b \rightarrow d\ell\ell$ and $s \rightarrow d\ell\ell$ process for this model. The crossed dots represent the effective $d_i \rightarrow d_j S$ vertex discussed in section 3.1.1. Similar diagrams can be drawn for up-quark FCNC processes.

propagator in powers of $\frac{q^2}{M_S^2}$. In such cases, we have to consider the Breit-Wigner (BW) propagator for S which is given by

$$\frac{i}{q^2 - M_S^2 + i\Gamma_s M_S}. \quad (4.1)$$

In this form of the propagator, we get a finite contribution from the propagator even at the resonance region. This is because, when $q^2 \approx M_S^2$, the leading effects will be from the imaginary part proportional to the S decay width. The imaginary part will receive contributions from every particle into which S can decay. Generally, without full knowledge of all possible decay channels for S , predicting its complete decay rate becomes challenging. Since here, the mass of the S is in GeV and sub-GeV range, the leading contribution to decay width comes from decay to leptons, light quarks, and DM χ . It cannot decay to heavy bosons like W , Z bosons, and also to the top-quark and Higgs bosons. For the decay of S to the SM fermions f , the decay widths $\Gamma(S \rightarrow f\bar{f})$ is defined as

$$\Gamma(S \rightarrow f\bar{f}) = N_c \frac{m_f^2 M_S}{8\pi} \left(1 - \frac{4m_f^2}{M_S^2}\right)^{1/2} \left[(c_s^2 + c_p^2) - \frac{4c_s^2 m_f^2}{M_S^2} \right], \quad (4.2)$$

where, $N_c = 3$ for decay to quarks and $N_c = 1$ for decay to leptons. The decay width of S to the dark fermion pair is given by :

$$\Gamma(S \rightarrow \bar{\chi}\chi) = \frac{M_S}{8\pi} \left(1 - \frac{4M_\chi^2}{M_S^2}\right)^{1/2} \left[(c_{s\chi}^2 + c_{p\chi}^2) - \frac{4c_{s\chi}^2 M_\chi^2}{M_S^2} \right]. \quad (4.3)$$

In this work, we have considered the contribution of our model to $B^0 - \bar{B}^0$, $B_s^0 - \bar{B}_s^0$ mixings. The contributions of our model to $D_0 - \bar{D}_0$ and $K_0 - \bar{K}_0$ mixings are CKM suppressed. Also, the contributions are loop-suppressed due to the small masses of the particle running in the loop. The relevant observable $\Delta M_{q'}$ (with $q' = d, s$) is defined as (for the mixing of $B_{q'}^0$ and $\bar{B}_{q'}^0$ mesons):

$$\Delta M_{q'} = 2|M_{12}^{q'}|, \quad (4.4)$$

where $M_{12}^{q'}$ is the amplitude of the mixing process and $M_{B_{q'}}$ is the mass of the neutral meson.

The frequencies of oscillations ΔM_s and ΔM_d have been measured by various experimental groups, the averages of which are given by [57, 111]:

$$\Delta M_s = 17.765 \pm 0.006 \text{ ps}^{-1}, \quad (4.5a)$$

$$\Delta M_d = 0.5065 \pm 0.0019 \text{ ps}^{-1}. \quad (4.5b)$$

The predictions in the SM are given by [58]:

$$\begin{aligned} \Delta M_s^{SM} &= 2|(M_{12}^s)_{SM}| = 18.23 \pm 0.63 \text{ ps}^{-1}, \\ \Delta M_d^{SM} &= 2|(M_{12}^d)_{SM}| = 0.535 \pm 0.021 \text{ ps}^{-1}. \end{aligned} \quad (4.6a)$$

The SM predictions have relatively large errors, and they are fully consistent with their respective measured values. Given the error in the estimates, there is still room for NP effects in these observables.

Taking into account the contributions from BSM physics, we can write the total oscillation frequency as

$$\Delta M_{q,tot} = 2|M_{12}^{q',SM} + M_{12}^{q',NP}| = \Delta M_{q',SM} |\Delta_{q'}|, \quad (4.7)$$

with

$$|\Delta_{q'}| = \frac{\Delta M_{q,tot}}{\Delta M_{q',SM}} = \left| 1 + \frac{M_{12}^{q',NP}}{M_{12}^{q',SM}} \right|. \quad (4.8)$$

In our model, the contribution in $(M_{12}^{q'})_{NP}$ is given by

$$\begin{aligned} M_{12}^{q',NP} &= 4G_F^2 M_W^2 (V_{tb} V_{tq'}^*)^2 \left(\frac{1}{16\pi^2} \right)^2 \frac{M_{B_{q'}}^2}{(m_b + m_{q'})^2} M_{B_{q'}}^2 f_{B_{q'}}^2 \eta_B \frac{1}{q^2 - M_S^2 + i\Gamma_S M_S} \times \\ &\quad \left(-\frac{5}{12} B_2 (C_1^2 m_{q'}^2 + C_2^2 m_b^2) + \frac{1}{2} B_4 m_b m_{q'} (C_1 C_2 + C_2 C_1) \right). \end{aligned} \quad (4.9)$$

B_2 , B_4 can be found from [56]. C_1 , C_2 are the loop contribution given in eq. (3.2). In the $\Delta_{q'}$, the sources of the mixing phases in the SM and the BSM scenarios are identical, which is the CKM matrix, and it cancels. However, due to the imaginary component of the BW propagator, $\Delta_{q'}$ will have a phase. As we will see later, this phase will be negligibly small since the total decay width Γ_S will be small due to the small allowed values of c_s and c_p .

Using the measured and the SM predicted values of ΔM_q , we have obtained the following allowed values of $\Delta_{q'}$:

$$|\Delta_d| = 0.9467 \pm 0.0373, \quad |\Delta_s| = 0.9746 \pm 0.0337. \quad (4.10)$$

We have used these two inputs to extract the coefficients c_s , c_p , and c_G .

4.1.2 Rare Decays of Mesons

Rare di-leptonic decays of neutral pseudoscalar mesons are important for probing new physics since the rate of these decays is suppressed in the SM. In this study, we primarily focus on FCNC processes, like $b \rightarrow s\mu^+\mu^-$, $b \rightarrow d\mu^+\mu^-$, $s \rightarrow d\mu^+\mu^-$. Examples of such decays include $B_s^0 \rightarrow \mu^+\mu^-$, $B^0 \rightarrow \mu^+\mu^-$, $K_{L,S} \rightarrow \mu^+\mu^-$. Decay to other leptons like electron and tau is also possible depending on the kinematics. For decay to tau, only the upper bound of the branching ratio is available, whereas, for electron, the branching ratio for our case will be very suppressed as the effect of considering MFV type coupling. Our model contributes to these processes via the diagram shown in Fig. 3b. Experimental data on respective branching ratios are available from different collaborations, like Belle-II, LHCb, ATLAS, and CMS. Following are the experimental data of the branching ratios are [59–61]:

$$\begin{aligned}\mathcal{B}(B_s^0 \rightarrow \mu^+\mu^-) &= (3.09_{-0.43}^{+0.46} \text{ }_{-0.11}^{+0.15}) \times 10^{-9}, \\ \mathcal{B}(B^0 \rightarrow \mu^+\mu^-) &= (0.12_{-0.07}^{+0.08} \pm 0.01) \times 10^{-9}, \\ \mathcal{B}(K_L \rightarrow \mu^+\mu^-) &= (6.84 \pm 0.11) \times 10^{-9}, \\ \mathcal{B}(K_S \rightarrow \mu^+\mu^-) &< 2.1 \times 10^{-10}.\end{aligned}\tag{4.11}$$

The SM contribution will be dependent only on C_{10} , including the QED corrections the SM predictions are given as [62]:

$$\mathcal{B}(B_s^0 \rightarrow \mu^+\mu^-) = (3.66 \pm 0.14) \times 10^{-9},\tag{4.12a}$$

$$\mathcal{B}(B^0 \rightarrow \mu^+\mu^-) = (1.03 \pm 0.05) \times 10^{-10}.\tag{4.12b}$$

Note that these SM predictions are fully consistent with the respective measurements shown in eq. (4.11). The expression of the branching ratios of the B and K mesons can be found in our previous work [56]. We have excluded processes such as $c \rightarrow u\mu^+\mu^-$ from our analysis due to CKM factors' suppression of the new physics amplitude and the masses of loop particles, as mentioned previously.

Furthermore, we have the available data in the processes related to $b \rightarrow s\ell\ell$ transitions. Plenty of data is available in $B \rightarrow K\mu^+\mu^-$, $B \rightarrow K^*\mu^+\mu^-$ and $B_s \rightarrow \phi\mu^+\mu^-$ decays; for example, see the refs. [40, 41, 63–66]. We have utilized all these data to constrain the new couplings. The detailed methodology and the inputs of this global analysis can be seen in our earlier publications [43, 56, 67].

The low energy effective Hamiltonian describing the $b \rightarrow s\ell^+\ell^-$ transitions is [68, 69]

$$\mathcal{H}_{eff} = -\frac{4G_F}{\sqrt{2}}V_{tb}V_{ts}^* \left[\sum_{i=1}^6 C_i(\mu)\mathcal{O}_i(\mu) + \sum_{i=7,8,9,10,P,S} \left(C_i(\mu)\mathcal{O}_i + C'_i(\mu)\mathcal{O}'_i \right) \right],\tag{4.13}$$

The parameters, operators and Wilson coefficients are described in the above references.

As previously discussed, the contribution to $b \rightarrow s\ell^+\ell^-$ processes in our model arises from the diagrams shown in Fig. 3b, where d_i is replaced by b and d_j by s . The amplitude of these diagrams depends on the effective $b \rightarrow sS$ vertex defined earlier and the lepton vertex factor, which is determined through the interaction.

$$\mathcal{L}_{\ell\ell S}^{int} = -m_\ell \bar{\ell}(c_s + ic_p \gamma_5)\ell. \quad (4.14)$$

To estimate the NP contributions in $b \rightarrow s\ell^+\ell^-$ decays, we need to use eqs. (3.1) and (4.14), respectively. The contribution we obtain from the diagram of Fig. 3b:

$$\begin{aligned} \mathcal{H}_{eff}^{NP} = \frac{g^2 V_{ts}^* V_{tb}}{32\pi^2} & \left(C_1 [\bar{s}(m_s P_L + m_b P_R)b] + C_2 [\bar{s}(m_s P_L - m_b P_R)b] \right) \times \\ & \frac{m_\ell}{q^2 - M_S^2 + i\Gamma_s M_S} \left(c_s [\bar{\ell}\ell] + ic_p [\bar{\ell}\gamma_5\ell] \right). \end{aligned} \quad (4.15)$$

A direct comparison of this equation with the most general effective Hamiltonian given in eq. (4.13), we will get

$$\begin{aligned} C'_S &= \frac{M_W^2 m_\ell m_s}{e^2 m_b} \frac{c_s (C_1(\Lambda) + C_2(\Lambda))}{q^2 - M_S^2 + i\Gamma_s M_S}, & C_S &= \frac{M_W^2 m_\ell}{e^2} \frac{c_s (C_1(\Lambda) - C_2(\Lambda))}{q^2 - M_S^2 + i\Gamma_s M_S}, \\ C'_P &= \frac{M_W^2 m_\ell m_s}{e^2 m_b} \frac{(ic_p)(C_1(\Lambda) + C_2(\Lambda))}{q^2 - M_S^2 + i\Gamma_s M_S}, & C_P &= \frac{M_W^2 m_\ell}{e^2} \frac{(ic_p)(C_1(\Lambda) - C_2(\Lambda))}{q^2 - M_S^2 + i\Gamma_s M_S}. \end{aligned} \quad (4.17)$$

Therefore, in our working model, the contributions in $b \rightarrow s\ell^+\ell^-$ will be via the four operators $\mathcal{O}_{S,P}$ and $\mathcal{O}'_{S,P}$. Note that all these four operators will contribute to the rates of $B \rightarrow K^{(*)}\mu^+\mu^-$ and $B_s \rightarrow \phi\mu^+\mu^-$ decays. In the next section, we will discuss the constraints from a global analysis of all the data available in $b \rightarrow s\mu^+\mu^-$ processes.

4.1.3 Fix Target Experiment

Light spin-0 particles can be produced directly (through gluon fusion) and indirectly (from meson decays) in fixed target experiments. There are some proton beam-dump results available, like CHARM [70], NuCal [71], and E613 [72]. We have taken the constraints from CHARM. Here, we will discuss the production via meson decays. This spin-0 particle can be produced from either K-meson or B-meson (production from D-meson decays is not considered here due to CKM and loop particle mass suppression). In the mass range $M_S \leq (M_K - M_\pi) \sim 0.36$ GeV, production from kaon decays dominate. For 0.36 GeV $\leq M_S \leq M_B$ mass range, decays dominate from B-meson. When the spin-0 particle is produced from K_L, K^+, B meson and decays into $e^+e^-, \mu^+\mu^-$ and $\gamma\gamma$, then the constraint from CHARM is important. Originally, CHARM had not detected any event. So, we have taken a bound at 90% confidence level of $N_{det} < 2.3$ events [73]. The production cross-section of spin-0 particle is given by :

$$\sigma_S \sim \sigma_{pp} M_{pp} \left(\frac{1}{14} \mathcal{B}(K^+ \rightarrow \pi^+ + S) + \frac{1}{28} \mathcal{B}(K_L \rightarrow \pi^0 + S) + 3 \times 10^{-8} \mathcal{B}(B \rightarrow X + S) \right). \quad (4.18)$$

The expressions for branching ratios are given in the previous discussion in eq. (4.39a). Here, the proton-proton cross-section is given by $\sigma_{pp} \simeq 40$ mbarn and the average hadron multiplicity $M_{pp} = 13$, for the CNGS beam. We can normalise the cross-section to the neutral pion yield by using $\sigma_{\pi_0} \approx \sigma_{pp} M_{pp} / 3$ [28]. The number of spin-0 particle produced

in the detector solid angle is expressed as $N_S \approx 2.9 \times 10^{17} \frac{\sigma_S}{\sigma_{\pi_0}}$ [74]. The number of events in the detector region is

$$N_{det} \sim N_S \left[\exp\left(\frac{-L_1}{\gamma \beta c \tau_S}\right) - \exp\left(\frac{-L_2}{\gamma \beta c \tau_S}\right) \right] \sum_{X=e,\mu,\gamma} Br(S \rightarrow XX). \quad (4.19)$$

Here, $L_1 = 480 \text{ m}$, the distance of the detector from the beam dump, and the difference $L_2 - L_1 = 35 \text{ m}$ is the detector's length. The typical relativistic factor is $\gamma \beta c = \frac{10}{M_S}$ and the lifetime of S is given by $\tau_S = \frac{1}{\Gamma_S}$. The expressions for branching ratios of S are given in the previous discussion in eqs. (4.2) and (4.3). The allowed parameter space for this case will be discussed in the next section.

4.1.4 Invisible Decays of Mesons

Recently Belle-II collaboration has provided the data on branching ratio of the decay $B^+ \rightarrow K^+ \nu \bar{\nu}$ which has 2.8σ discrepancies with SM. This significance was obtained under the assumption of heavy NP [46]. Similarly, data or upper bounds are available on a few other invisible decay channels like $B \rightarrow K^{(*)} \nu \bar{\nu}$, $B \rightarrow \rho \nu \bar{\nu}$, $K \rightarrow \pi \nu \bar{\nu}$. We have shown the available data or the upper limits on the respective channels in Table 1.

Decays like $B \rightarrow K \nu \bar{\nu}$, $K \rightarrow \pi \nu \bar{\nu}$, which contains neutrinos as final state particles, are treated as invisible decays in SM since they are not detectable and experimental bounds come from treating them as missing energy. So, instead of ν , if we have any other long-lived particle, we will have the same experimental signature. In the model we have considered, we do not have any coupling of the SM neutrino with the mediator as they are generally massless in SM, but the spin-0 mediator can interact with the DM χ . So the signature of the decay $P \rightarrow P' \chi \bar{\chi}$ will have a similar experimental signature as $P \rightarrow P' \nu \bar{\nu}$. Here P and P' stands for pseudoscalar or vector mesons. The DM χ will have a mass in the kinematically allowed region: $M_\chi \leq \frac{M_P - M_{P'}}{2}$. The measured branching fraction of $P \rightarrow P' \nu \bar{\nu}$ decay can be expressed as:

$$Br[P \rightarrow P' \nu \bar{\nu}]_{Exp} = Br[P \rightarrow P' \nu \bar{\nu}]_{SM} + Br[P \rightarrow P' + \chi \bar{\chi}]_{NP}, \quad (4.20)$$

Here, the NP and SM contribution will be added in the decay width order as the available phase space for these two decays is different.

Apart from the $P \rightarrow P' \chi \bar{\chi}$ three-body decay, the analysis of $P \rightarrow P' \nu \bar{\nu}$ decays are potentially sensitive to the process $P \rightarrow P' + S$. Here, S is our spin-0 mediator, have mass in the region $M_S \leq (M_P - M_{P'})$. Therefore, S can be produced on-shell and can decay almost entirely to DM particle. In that case, the experimental measurement of invisible decay can be seen as:

$$Br[P \rightarrow P' \nu \bar{\nu}]_{Exp} = Br[P \rightarrow P' \nu \bar{\nu}]_{SM} + Br[P \rightarrow P' + S], \quad (4.21)$$

So, which kind of decay we get, will actually depend on whether the mediator can be produced on-shell or not. If it can be produced off-shell, then we get the signature of $P \rightarrow P' \chi \bar{\chi}$ three-body decay. However, if it is on-shell, then this decay can be considered as $P \rightarrow P' S (\rightarrow \chi \bar{\chi})$. The Belle-II experimental data on $B \rightarrow K \nu \bar{\nu}$ is provided under the

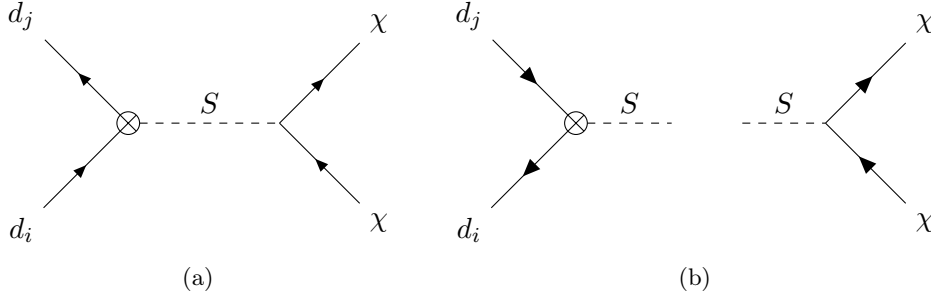


Figure 4. (a) Feynman diagram contributing to the three body $P \rightarrow P' \bar{\chi} \chi$ decays. The crossed dot denotes the effective vertex coming from the 1-loop correction. (b) Feynman diagram contributing to the invisible decay process $P \rightarrow P' S (S \rightarrow \bar{\chi} \chi)$ via on-shell S .

assumption of a heavy new particle, which will be accurate for the first scenario. Below, we will discuss both type of decay and their branching ratio in this simplified model.

Decay via Virtual Mediator S : First, we discuss the three-body decay $P \rightarrow P' \bar{\chi} \chi$ where spin-0 mediator S will be an off-shell propagator. A representative Feynman diagram of such a process is given in fig 4a. For the decay of B meson (both charged and neutral), the underlying quark interaction process is $b \rightarrow s(d) \bar{\chi} \chi$ and the same for K-meson is $s \rightarrow d \chi \bar{\chi}$. For the decay $P \rightarrow P' \chi \bar{\chi}$ to be kinematically allowed, we will have the bound on the fermionic dark matter mass: $2m_\chi \leq (M_P - M_{P'})$.

For the decay $B \rightarrow K \chi \bar{\chi}$, the amplitude will be calculated from the diagram 4a which is given by

$$\begin{aligned} \mathcal{M} &= \frac{g^2 V_{tb} V_{ts}^*}{32\pi^2} \frac{(C_1(\Lambda)(m_b + m_s) + C_2(\Lambda)(m_b - m_s))}{\sqrt{(M_B^2/2 - M_S^2)^2 + \Gamma_S^2 M_S^2}} \langle K | \bar{s} b | B \rangle (\bar{\chi} (c_{s\chi} + i c_{p\chi} \gamma_5) \chi), \\ &= (C_L + C_R) \langle K | \bar{s} b | B \rangle (\bar{\chi} (c_{s\chi} + i c_{p\chi} \gamma_5) \chi). \end{aligned} \quad (4.22)$$

with

$$C_L = \frac{g^2 V_{ts}^* V_{tb} (m_b + m_s)}{32\pi^2 \sqrt{(M_B^2/2 - M_S^2)^2 + \Gamma_S^2 M_S^2}} C_1(\Lambda), \quad C_R = \frac{g^2 V_{ts}^* V_{tb} (m_b - m_s)}{32\pi^2 \sqrt{(M_B^2/2 - M_S^2)^2 + \Gamma_S^2 M_S^2}} C_2(\Lambda). \quad (4.23)$$

Here, C_1 and C_2 are the effective vertex factors for $b \rightarrow sS$ vertex, given in Sec. 3.1.1. The $B \rightarrow K$ transition matrix element is defined via the QCD form factor $f_0(q^2)$

$$\langle K | \bar{s} b | B \rangle = \frac{M_B^2 - M_K^2}{m_b - m_s} f_0(q^2). \quad (4.24)$$

Similarly, we can express the amplitude of $B \rightarrow K^* \chi \bar{\chi}$ decay using the QCD form factors and C_L and C_R .

The differential decay rate distribution for $B \rightarrow K^{(*)} \chi \bar{\chi}$ decay can be expressed as

$$\frac{d\Gamma_{B \rightarrow K^{(*)} \chi \bar{\chi}}}{dq^2} = \frac{1}{32M_B^3} \frac{1}{(2\pi)^3} \frac{\lambda^{1/2}(M_\chi^2, M_\chi^2, q^2)}{q^2} \lambda^{1/2}(M_B^2, M_{K^{(*)}}^2, q^2) \left| \mathcal{M}_{B \rightarrow K^{(*)} \chi \bar{\chi}} \right|^2, \quad (4.25)$$

Branching Ratio	SM Value	Experimental Value
$B^+ \rightarrow K^+ \nu \bar{\nu}$	$((5.06 \pm 0.14 \pm 0.28)) \times 10^{-6}$ [75]	$(2.3 \pm 0.5_{-0.4}^{+0.5}) \times 10^{-5}$ [46]
$B_0 \rightarrow K_S^0 \nu \bar{\nu}$	$(2.05 \pm 0.07 \pm 0.12) \times 10^{-6}$ [75]	$< 1.3 \times 10^{-5}$ [50]
$B^+ \rightarrow K^{*+} \nu \bar{\nu}$	$((10.86 \pm 1.30 \pm 0.59)) \times 10^{-6}$ [75]	$< 6.1 \times 10^{-5}$ [50]
$B_0 \rightarrow K^{*0} \nu \bar{\nu}$	$(9.05 \pm 1.25 \pm 0.55) \times 10^{-6}$ [75]	$(3.8_{-2.6}^{+2.9}) \times 10^{-5}$ [52] $< 1.8 \times 10^{-5}$ [50]
$B^+ \rightarrow \pi^+ \nu \bar{\nu}$	$(1.57 \pm 0.44) \times 10^{-7}$ [76]	$< 1.4 \times 10^{-5}$ [50]
$B_0 \rightarrow \pi^0 \nu \bar{\nu}$	$(0.73 \pm 0.21) \times 10^{-7}$ [76]	$< 0.9 \times 10^{-5}$ [50]
$B^+ \rightarrow \rho^+ \nu \bar{\nu}$	$(3.92 \pm 0.79) \times 10^{-7}$ [76]	$< 3 \times 10^{-5}$ [50]
$B_0 \rightarrow \rho^0 \nu \bar{\nu}$	$(1.82 \pm 0.31) \times 10^{-7}$ [76]	$< 4 \times 10^{-5}$ [50]
$K^+ \rightarrow \pi^+ \nu \bar{\nu}$	$(8.60 \pm 0.42) \times 10^{-11}$ [77]	$(1.06_{-0.34}^{+0.40} \pm 0.09) \times 10^{-10}$ [53]
$K_L \rightarrow \pi^0 \nu \bar{\nu}$	$(2.94 \pm 0.15) \times 10^{-11}$ [77]	$< 2.2 \times 10^{-9}$ [78]

Table 1. Updated SM predictions and the measured values or upper limit on the branching ratios of the invisible decays of B and K mesons.

with

$$|\mathcal{M}_{B \rightarrow K^* \chi \bar{\chi}}(q^2)|^2 = \frac{(C_R - C_L)^2}{(m_b + m_s)^2} \lambda(M_B^2, M_{K^{(*)}}^2, q^2) A_0^2(q^2) [2q^2(c_{s\chi}^2 + c_{p\chi}^2) - 8c_{s\chi}^2 M_\chi^2], \quad (4.26a)$$

$$|\mathcal{M}_{B \rightarrow K \chi \bar{\chi}}(q^2)|^2 = (C_L + C_R)^2 \frac{(M_B^2 - M_K^2)^2}{(m_b - m_s)^2} f_0^2(q^2) [2q^2(c_{s\chi}^2 + c_{p\chi}^2) - 8c_{s\chi}^2 M_\chi^2]. \quad (4.26b)$$

Here, A_0 is the vector form factor defined as

$$\langle K^*(p, \eta) | \bar{s} \gamma_5 b | \bar{B}(p_B) \rangle = \left(\frac{2M_{K^*}(\eta^* \cdot q)}{i(m_s + m_b)} \right) A_0(q^2). \quad (4.27)$$

The form factors $f_0(q^2), A_0(q^2)$ are discussed in detail in next subsection. The Kallen function λ can be given by:

$$\lambda(a, b, c) = a^2 + b^2 + c^2 - 2ab - 2ac - 2bc. \quad (4.28)$$

The branching ratios depend on the couplings c_s, c_p , and c_G via C_1 and C_2 . Furthermore, these rates are sensitive to the coupling of DM-mediator interaction $c_{s\chi}, c_{p\chi}$ along with the DM mass, which has to be in the region mentioned above.

In order to obtain the decay rate distributions or the branching fractions, we need knowledge of the q^2 shapes of the associated form factors (FF). For the $B \rightarrow K$ process, the knowledge of $f_0(q^2)$ is required. Also, the symmetry relation among the matrix elements can be written as

$$\langle K_S | \bar{b} \gamma_\mu s | B^0 \rangle = -\langle K_S | \bar{s} \gamma_\mu b | \bar{B}^0 \rangle = \frac{1}{\sqrt{2}} \langle K^+ | \bar{s} \gamma_\mu b | \bar{B}^+ \rangle. \quad (4.29)$$

In BCL (Bourreley-Caprini-Lellouch) parametrization, the FF can be written as [79, 80]:

$$f_0(q^2) = \frac{\mathcal{L}}{1 - \frac{q^2}{M_{H_{s0}^*}^2}} \sum_{n=0}^{N-1} a_n^0 z^n. \quad (4.30)$$

This uses a mapping of q^2 to z so that the physical q^2 range $0 \leq q^2 \leq (M_B - M_K)^2$ is mapped to a region of unit circle in z

$$z(q^2, t) = \frac{\sqrt{t_+ - q^2} - \sqrt{t_+ - t_0}}{\sqrt{t_+ - q^2} + \sqrt{t_+ - t_0}}, \quad (4.31)$$

with $t_+ = (M_B + M_K)^2$. Here $t_0 = 0$ is set [80]. Here, $M_{H_{s0}^*}^2 = M_B + \Delta$, with $\Delta = 0.45 \text{ GeV}$. Expanding up to $N = 3$, fit results of the expansion coefficients and correlation among them are given in [80]. The coefficients are given by:

$B \rightarrow K$	
a_0^0	0.2545(90)
a_1^0	0.210(76)
a_2^0	0.02(17)

The FFs of $B \rightarrow K^*$ is obtained as

$$\langle K^*(p, \eta) | \bar{s} \gamma_5 b | \bar{B}(p_B) \rangle = \left(\frac{2M_{K^*}(\eta^* \cdot q)}{i(m_s + m_b)} \right) A_0(q^2). \quad (4.32)$$

Using a simplified series expansion, we have written the respective FFs as [81] :

$$F(t) = \frac{1}{P(t)} [a_0(1 + c_{01}\Delta x + c_{01s}\Delta x_s) + a_1 z] \quad (4.33)$$

where z has the same expression as in eq. (4.31) and written as $z(t, t_0)$, with $t_\pm = (M_B \pm M_{K^*})^2$, and $q^2 = t$. The pole factor is given as

$$P(t; \Delta m) = 1 - \frac{t}{(M_B + \Delta m)^2}. \quad (4.34)$$

We also have

$$\Delta x = \frac{M_\pi^2 - m_{\pi, \text{phys}}^2}{(4\pi f_\pi)^2}, \quad (4.35a)$$

$$\Delta x_s = \frac{(M_{\eta_s}^2 - M_{\eta_s, \text{phys}}^2)}{(4\pi f_\pi)^2}. \quad (4.35b)$$

Here, $f_\pi = 132\text{MeV}$ is used. Masses of the pseudoscalar and the physical masses are available in ref. [81]. The values of the coefficients $a_0, a_1, c_{01}, c_{01s}$ are also taken from [81].

For $B \rightarrow \rho$ FFs can be written in Simplified Series Expansion (SSE) [42]:

$$F(q^2) = P(q^2) \sum_k a_k [z(q^2) - z(0)]^k, \quad (4.36)$$

with $P(q^2) = (1 - q^2/M_{R,i}^2)^{-1}$, is a simple pole corresponding to the first resonance in the spectrum. For this case $M_{R,i} = 5.279$ GeV. The value of the coefficients a_i can be found from [42]. Furthermore, we have taken the inputs on $B \rightarrow \pi$ FFs from [82]. To obtain the $K \rightarrow \pi$ form factor, we have used the analysis given in ref. [83].

In the numerical analyses, for the three body decays $P \rightarrow P'\chi\bar{\chi}$, we have determined the allowed values of the branching ratios $\mathcal{B}(P \rightarrow P'\chi\bar{\chi})_{\text{NP}}$ from the differences of the respective measured and the SM predicted values, such as

$$\mathcal{B}(P \rightarrow P'\chi\bar{\chi})_{\text{NP}} = \mathcal{B}(P \rightarrow P'\nu\bar{\nu})_{\text{Exp}} - \mathcal{B}(P \rightarrow P'\nu\bar{\nu})_{\text{SM}}. \quad (4.37)$$

The respective values of $\mathcal{B}(P \rightarrow P'\nu\bar{\nu})_{\text{SM}}$ and $\mathcal{B}(P \rightarrow P'\nu\bar{\nu})_{\text{Exp}}$ are given in Table 1. Using these inputs, we have obtained the respective values of $\mathcal{B}(P \rightarrow P'\chi\bar{\chi})_{\text{NP}}$ which we have used further to constraints the new parameters of our simplified model.

Decay via Resonance S : We have mentioned that the analysis of $P \rightarrow P'\nu\bar{\nu}$ could be sensitive to the on-shell production of the new light boson S through the decay $P \rightarrow P'+S(\rightarrow \bar{\chi}\chi)$. The experimental upper limit of such processes is available for a few channels of B and K meson. Technically, the bound shall depend on the lifetime of the particle S . Hence, the branching ratio will be a function of the mass of S . The upper limit on branching ratios $\mathcal{B}(K^+ \rightarrow \pi^+ + S)$ and $\mathcal{B}(K_L \rightarrow \pi^0 + S)$ as a function of the mass of the invisible particle is given by KOTO [84] and Na62 [53], respectively. For $B \rightarrow K + S$ decay the branching ratio is provided by the experiment CLEO [85], and their result is valid only for the case when $M_S = 0$.

In ref. [54], the authors have reinterpreted the $B \rightarrow K^{(*)}\nu\bar{\nu}$ measurement as a search for the two-body $B \rightarrow K^{(*)}S$ decay with the assumption that the undetected particle S is stable (approximately) or decays invisibly. They used the differential distributions of the $B^{0,+} \rightarrow K^{0,+}\nu\bar{\nu}$ measurements of Belle II [46] and BaBar [52] and fitted the NP signal to reconstruct the data by modeling the resonance S with a Gaussian distribution. They have repeated this exercise for $B \rightarrow K^*\nu\bar{\nu}$ measurement by BaBar [52]. Finally, they have obtained a M_S dependent limits on the branching fractions $\mathcal{B}(B \rightarrow KS)$ and $\mathcal{B}(B \rightarrow K^*S)$, respectively. They have given 1σ and 2σ error with the best-fit value of the branching ratios, depending upon the mass of S . We have used these results to constrain the SDM parameters. Depending upon whether we take 1σ or 2σ error of the branching ratio, we get very different bounds on the parameter space while considering the decay with other constraints, which will be discussed in the next section. So, we will analyse by considering both 1σ or 2σ error of this decay. They have provided the branching ratio for $M_S \leq 3$ GeV. We will show later that these invisible channels greatly impact the parameter space. We will divide the parameter space into two regions viz $M_S \leq 3$ GeV and $M_S > 3$ GeV.

Allowing the mediator to decay to the dark fermion pair, we get the invisible signature from the decay $P \rightarrow P' \chi \bar{\chi}$. The branching ratio can be written as

$$\mathcal{B}(P \rightarrow P' \chi \bar{\chi}) = \mathcal{B}(P \rightarrow P' S) \times \mathcal{B}(S \rightarrow \chi \bar{\chi}). \quad (4.38)$$

Here, P' could be either a pseudoscalar or a vector meson with the following branching fractions

$$\mathcal{B}(P \rightarrow MS) = \frac{\tau_P}{16\pi M_P^3} \lambda^{1/2}(M_P^2, M_M^2, M_S^2) |\mathcal{M}_{P \rightarrow MS}(M_S^2)|^2 \quad (4.39a)$$

$$\mathcal{B}(P \rightarrow VS) = \frac{\tau_P}{16\pi M_P^3} \lambda^{1/2}(M_P^2, M_V^2, M_S^2) |\mathcal{M}_{P \rightarrow VS}(M_S^2)|^2 \quad (4.39b)$$

where M is a pseudoscalar and V is a vector meson. In our case, the amplitudes take the following forms

$$|\mathcal{M}_{P \rightarrow MS}(q^2)| = (C'_R + C'_L) \left(\frac{M_P^2 - M_M^2}{m_{d_i} - m_{d_j}} \right) f_0(q^2), \quad (4.40a)$$

$$|\mathcal{M}_{P \rightarrow VS}(q^2)| = (C'_R - C'_L) \frac{\lambda^{1/2}(M_P^2, M_V^2, q^2)}{(m_{d_i} + m_{d_j})} A_0(q^2). \quad (4.40b)$$

where,

$$C'_L = \frac{g^2 V_{ts}^* V_{tb}(m_b + m_s)}{32\pi^2} C_1(\Lambda), \quad C'_R = \frac{g^2 V_{ts}^* V_{tb}(m_b - m_s)}{32\pi^2} C_2(\Lambda). \quad (4.41)$$

Here,

$$\mathcal{B}(S \rightarrow \chi \bar{\chi}) = \frac{\Gamma(S \rightarrow \chi \bar{\chi})}{\Gamma(S \rightarrow \chi \bar{\chi}) + \Gamma(S \rightarrow f \bar{f})_{\text{SM}}} \quad (4.42)$$

$\Gamma(S \rightarrow f \bar{f})_{\text{SM}}$ denotes the sum of the decay width of S to all the possible SM fermions. The expression of the decay widths of mediator S to $f \bar{f}$ and to $\chi \bar{\chi}$ are given in eq. (4.3) and eq. (4.2), respectively.

4.2 FCCC Observables

In Sec. 4.2, we discussed how our model influences the effective vertices of FCCC. These corrections are significant for processes where the SM contribution arises from tree-level diagrams, such as semileptonic and leptonic decays involving B , B_s , and K mesons. As we will see later, for low mediator mass, the constraints from FCCC processes are relaxed as compared to the rare FCNC and invisible decays. So here, we will just name the possible observable to which this simplified model can contribute. The detailed discussion can be found in [56].

Anomalous Couplings of $t \rightarrow bW$ Decay : The general Lagrangian for $t \rightarrow bW_\mu^-$ decay is given by [86, 87]:

$$\mathcal{L}_{tWb} = -\frac{g}{\sqrt{2}} \bar{b} \gamma_\mu (V_L P_L + V_R P_R) t W_\mu^- - \frac{g}{\sqrt{2}} \bar{b} \frac{i\sigma_{\mu\nu} q_\nu}{M_W} (g_L P_L + g_R P_R) t W_\mu^- + h.c. \quad (4.43)$$

$V_{L(R)}$, $g_{L(R)}$ are known as the anomalous couplings. In Standard Model, we have $V_L = V_{tb}^*$ and V_R , g_L , $g_R = 0$. The experimental constraints on these couplings are provided by ATLAS [88] and CMS [86, 87, 89], as given in Table 3 of ref. [56]. In this model we get,

$$\begin{aligned} V_R &= V_{tb}^* C_{VR}, \\ V_L &= V_{tb}^* (1 + C_{VL}). \end{aligned} \quad (4.44)$$

$C_{VL(R)}$ are shown in eq. (3.3). The contributions to g_L and g_R will be negligibly small compared to V_R or V_L , hence we ignored that.

Semi-leptonic and Leptonic Decays of Mesons : The corrections to the SM charged current vertices will impact the semileptonic and leptonic decays of B , B_s , K , D , and D_s mesons. The most general Hamiltonian that contains all possible four fermion operators of lowest dimension for $d_j \rightarrow u_i \ell \bar{\nu}$ can be written as

$$\mathcal{H}_{eff} = \frac{4G_F}{\sqrt{2}} V_{u_i d_j} [(1 + C_{VL}) \mathcal{O}_{VL} + C_{VR} \mathcal{O}_{VR}]. \quad (4.45)$$

The four-fermi operators are given by

$$\begin{aligned} \mathcal{O}_{VL} &= (\bar{u}_{iL} \gamma^\mu d_{jL})(\bar{\ell}_L \gamma_\mu \nu_{\ell L}), \\ \mathcal{O}_{VR} &= (\bar{u}_{iR} \gamma^\mu d_{jR})(\bar{\ell}_L \gamma_\mu \nu_{\ell L}). \end{aligned} \quad (4.46)$$

For a detailed discussion, please refer to [56]. The contribution of NP to the branching ratio of the decays $P \rightarrow M \ell \nu$ and $P \rightarrow \ell \nu$ can be considered as the modification of the CKM matrix elements: $|V'_{u_i d_j}| = |V_{u_i d_j} (1 + C_{VL} \pm C_{VR})|$. From the experimental data, CKM elements can be extracted, i.e., NP can be constrained [90]. Since, for the low mass of the mediator FCCC constraints will not play a vital role, we will skip that part here.

4.3 Electroweak Precision Observables

The precise measurements of electroweak precision observables (EWPO) at the W and Z poles allow us to impose constraints on new physics scenarios. This is achieved by analyzing how new physics contributions at the loop level affect these electroweak observables. Here, We will just summarise the observables we have taken. The detail discussion on the loop contribution and the observables are given in ref. [56].

Oblique Parameters: The observable taken here is :

$$\delta(\Delta r) = (\Delta r)_{Exp} - (\Delta r)_{SM}, \quad (4.47)$$

which is related to the mass of the gauge boson as:

$$M_W^2 \left(1 - \frac{M_W^2}{M_Z^2} \right) = \frac{\pi \alpha_{em}}{\sqrt{2} G_F} \frac{1}{1 - \Delta r}. \quad (4.48)$$

Depending upon different experimental values of M_W (given by LHCb [91], ATLAS [92], D0 [93], CDF [94], CMS [134]), we can calculate the values of $\delta(\Delta r)$. Among all these data, only the CDF data has a $\approx 7\sigma$ discrepancy with the SM whereas the other data are consistent. In our previous work [56], we discussed the results separately due to the effect of adding CDF data to analysis. In this work, we will not include the CDF data in our analysis.

Z Pole Observables : This model will contribute to the decay of Z boson via penguin loop diagram; the corresponding diagrams can be found in Fig. 9 of [56]. Z bosons interact with the SM fermions via vector and axial couplings. After inserting the loop diagrams, the couplings will be modified:

$$\begin{aligned} g_{af} &\rightarrow a_f + \Delta a_f^{NP}, \\ g_{vf} &\rightarrow v_f + \Delta v_f^{NP}. \end{aligned} \quad (4.49)$$

LEP and SLAC measured various branching ratios to have better control on systematic uncertainties. These measurements include different observables related to this process, commonly referred to as the Z -pole observables, which have been determined with fairly good accuracy [59]. Among these observables, we have focused on the following decay rate ratios [95, 96]:

$$R_\ell = \frac{\Gamma_{had}}{\Gamma_\ell}, \quad R_c = \frac{\Gamma_c}{\Gamma_{had}}, \quad R_b = \frac{\Gamma_b}{\Gamma_{had}}. \quad (4.50)$$

We have $\Gamma_{had} = \Gamma_u + \Gamma_d + \Gamma_s + \Gamma_c + \Gamma_b$. The expression in terms of our model parameters is given in Sec. 3 of [56]. The SM values are given below [59, 97] :

$$\begin{aligned} R_e^{SM} &= 20.736 \pm 0.010, & R_\mu^{SM} &= 20.736 \pm 0.010, & R_\tau^{SM} &= 20.781 \pm 0.010, \\ R_b^{SM} &= 0.21582 \pm 0.00002, & R_c^{SM} &= 0.17221 \pm 0.00003. \end{aligned} \quad (4.51)$$

The experimental values corresponding to these observables can be found in [59], also in Table 3. We also have considered asymmetry observables like A_τ , A_μ , A_e , A_b and A_c with value:

$$A_f = 2 \frac{g_{af} g_{vf}}{g_{af}^2 + g_{vf}^2}, \quad (4.52)$$

More details on these are discussed in [56].

4.4 Cosmological Constraints

Apart from the constraints coming from flavour physics and the W and Z -pole observables, we also have studied cosmological constraints. Below we discuss constraints coming from Big Bang Nucleosynthesis and the condition of thermal equilibrium, which sets a lower limit on the couplings in parameter space.

Big Bang Nucleosynthesis : Suppose the dominant decay modes of the DM is into spin-0 particles. In that case, these spin-0 particles need to decay rapidly enough before Big Bang Nucleosynthesis (BBN) to prevent changes in the expansion rate and the entropy density during BBN or the destruction of certain elements. Being long-lived, the spin-0 particle S may affect the universe's early history. If S had been in thermal equilibrium and decayed around or later than about a second after the Big Bang, the produced particles would affect BBN [98, 99]. Although calculating precise constraints is challenging, such constraints become less significant if the average lifetime of the spin-0 particle is less than 1 second. However, the constraints are severe for very small masses of S and become less constraining for higher masses. The expression for the decay width of the spin-0 mediator is

discussed previously in eq. (4.3). This constraint will give us a lower limit on the couplings of our interest. As can be seen from the expression of decay width, with increasing the mass of the mediator, decay width increases. That is why constraint is more important for the lower mass region of the mediator.

Thermal Equilibrium : In our working model, we have considered a fermion χ , which is a DM candidate and is expected to reproduce the correct relic density of the Universe via the freeze-out method. For the DM to freeze out, it should be primarily in the thermal equilibrium with the SM in the early universe. So, if the interaction rate of the DM with the SM particles is very small, it cannot be in the thermal equilibrium. The interaction of the DM with SM particles is governed by the couplings c_s, c_p in our working model. These couplings can not be very small for the DM to be in thermal equilibrium. Here, we will discuss the lower limit on the couplings. Certainly, the dark sector could undergo thermalisation if the couplings $c_{s\chi}$ and $c_{p\chi}$ are large. However, it is likely to possess a temperature different from that of the visible sector. The DM could still undergo freeze-out into spin-0 particles, but the resulting abundance becomes dependent on the specifics of reheating. If all the couplings are very small, DM can no longer produce observed relic density via freeze-out; it can be obtained through the freeze-in method.

For the DM to be in thermal equilibrium, we know, the interaction rate has to be larger than the expansion rate of the universe :

$$\langle\sigma v\rangle n_{\text{eq}} > H, \quad (4.53)$$

where H is the Hubble rate: $H = 1.66\sqrt{g_*}T^2/M_P$, M_P being the Planck mass and g_* is the d.o.f. n_{eq} is the equilibrium number density. $\langle\sigma v\rangle$ can be given by either the production of SM particles from SM annihilation or vice versa. DM can annihilate to various particles of SM.

$$\langle\sigma v\rangle n_{\text{eq}} = \sum_{X=f,V} \langle\sigma v\rangle_{\bar{\chi}\chi\rightarrow XX} n_{\text{eq}}^X \quad (4.54)$$

Here, X stands for SM fermions and vector bosons. We can write:

$$\langle\sigma v\rangle_{\bar{\chi}\chi\rightarrow XX} n_{\text{eq}}^X = \frac{1}{8\pi^2 M_\chi^2 K_2(M_\chi/T)} \int_{s_{\text{min}}}^{\infty} ds \sigma_{\bar{\chi}\chi\rightarrow XX} (s - 4M_\chi^2) \sqrt{s} K_1(\sqrt{s}/T), \quad (4.55)$$

K_i 's are the modified Bessel functions of the second kind and the expression for $\sigma_{\bar{\chi}\chi\rightarrow\bar{f}f}$ can be found in appendix E of [56].

4.5 DM Constraints

As mentioned in Sec. 2, we have considered a fermionic DM χ which is communicating with the SM particles via a spin-0 mediator S . Here we have taken χ to be a WIMP type DM, whose stability can be described by imposing a \mathbb{Z}_2 symmetry on it to prevent it from decaying. The DM generates the observed relic density [100] via s-channel and t-channel annihilation diagrams. The dominating annihilation channels are $\chi\bar{\chi} \rightarrow f\bar{f}, SS$, where f stands for SM fermions. Another loop-generated annihilation channel will be $\chi\bar{\chi} \rightarrow gg$, which is coming from a top-quark mediated penguin loop. All the relevant diagrams are

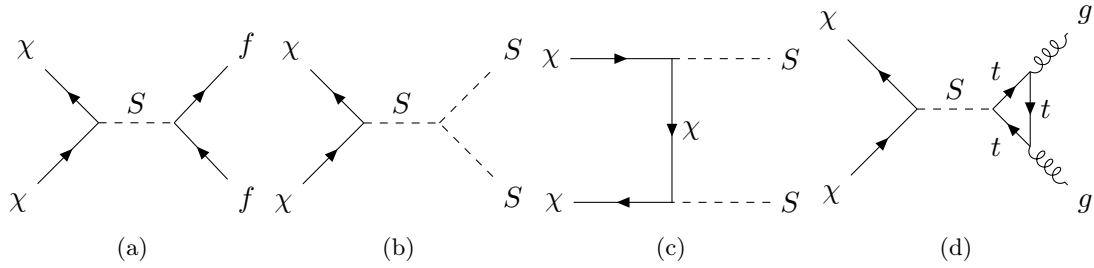


Figure 5. Feynman diagrams depicting the annihilation channels of the DM are significant for determining relic density.

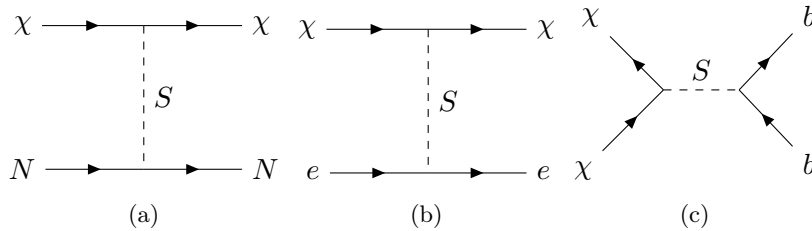


Figure 6. Feynman diagrams contribute to the direct detection process, DM-electron scattering process, and to the indirect detection for annihilation to $b\bar{b}$ (right).

the same as in [56]. Since, in this study, we are mainly interested in comparatively lower mass DM with mass $M_\chi \leq 10$ GeV, the annihilation process $\chi\bar{\chi} \rightarrow t\bar{t}, VV$, where V stands for SM vector bosons, will not contribute to relic density. So, for $M_\chi \leq M_S$, the dominating channel will be $\chi\bar{\chi} \rightarrow b\bar{b}$ and for $M_\chi \geq M_S$, the dominating channel will be $\chi\bar{\chi} \rightarrow SS$ via both s-channel and t-channel diagrams. Also, for very small c_s, c_p , annihilation to spin-0 mediator will be the only process that contributes significantly to relic density.

Fig. 5 shows the Feynman diagrams of annihilation of the DM, which can annihilate to SM or another dark sector particle via s-channel or t-channel annihilation diagrams. It will mainly annihilate to SM fermion pair $\bar{f}f$ via an s-channel diagram for $M_\chi \geq m_f$. Hence, it cannot annihilate to top-quark pair. The next dominating process will be annihilation to $b\bar{b}$ pair. Although in our simplified model, we have couplings of spin-0 mediator with the SM gauge boson, here, DM cannot annihilate to SM gauge boson due to kinematical constraint. There will be a large annihilation cross-section of $\chi\bar{\chi} \rightarrow gg$ via a top-penguin diagram, resulting in a considerable contribution to $\langle\sigma v\rangle$. The effective vertex of this process is given following:

$$\mathcal{L}_{gluon} = \frac{\alpha_s}{8\pi} \left(c_s \tau [1 + (1 - \tau)f(\tau)] G^{\mu\nu} G_{\mu\nu} + 2c_p \tau f(\tau) G^{\mu\nu} \tilde{G}_{\mu\nu} \right) S, \quad (4.56)$$

Where, $\tau = \frac{4m_t^2}{M_S^2}$ and

$$f(\tau) = \begin{cases} \arcsin^2 \frac{1}{\sqrt{\tau}} & \text{if } \tau \geq 1 \\ -\frac{1}{4} \left(\log \frac{1+\sqrt{1-\tau}}{1-\sqrt{1-\tau}} - i\pi \right)^2 & \text{if } \tau < 1 \end{cases}$$

The processes mentioned above apply to any mass M_S of the spin-0 mediator. But for the case $M_S \leq M_\chi$, another channel will open up $\chi\bar{\chi} \rightarrow SS$ via an s-channel as well as t-channel diagram as shown in figs. 5b and 5c. The t-channel diagram will have a significant contribution to the relic, especially in the case of very small c_s and c_p ; it will be governed by the couplings $c_{s(p)\chi}$.

In our scenario, the parameter space could also be constrained from the t-channel DM-nucleon scattering process $\chi N \rightarrow \chi N$. The upper bounds on the DM-nucleon scattering cross-section are provided by various experiments: XENONnT [101], LUX-ZEPLIN [102], and PandaX-4T [103], etc. The direct detection bound given by the above experiments is mostly effective for DM mass $M_\chi \gtrsim 5$ GeV, and the bound is sensitive to the DM and mediator masses. The most stringent bound comes from LUX-ZEPLIN [102], which gives $\langle\sigma v\rangle \sim 10^{-46} \text{ cm}^2$ for $M_\chi \sim 10$ GeV while for $M_\chi \sim 5$ the cross-section is of order 10^{-44} cm^2 [102]. The DD bound on nucleon scattering cross-section for the sub-GeV DM is given by the experiments as: XENONnT [104], DarkSide-50 [105], SENSEI [106], PandaX-4T [107], LZ [108], SuperCDMS [109], LUX [110]. For $2 \lesssim M_\chi \lesssim 5$ GeV the cross-section $\langle\sigma v\rangle \sim 1.4 \times 10^{-42} \text{ cm}^2$ which is obtained from DarkSide-50 [105, 111]. While for $M_\chi < 2$ GeV, the bounds are relatively relaxed, and the cross-section $\langle\sigma v\rangle$ will be in the range 10^{-37} cm^2 to 10^{-39} cm^2 . In our analysis, we have used these mass-dependent bounds. The expression for the spin-independent direct detection cross-section is given in Appendix E of [56], where the dependency of the cross-section can be seen as (at $t \rightarrow 0$ limit):

$$\sigma_{\chi N}^{SI} \propto \frac{c_{s\chi}^2 c_s^2}{M_S^4}. \quad (4.57)$$

An alternative way to search for a light DM candidate is through the scattering of electrons, i.e., $DM + e \rightarrow DM + e$ [112, 113]. The experimental and the proposed bounds on the cross-section for this process is given by various proposed and ongoing experiments like: XENON100 [114], CRESST-III [115], DAMIC-M [116], DarkSide-50 [117], ALETHEIA [118], DarkSide-20k [119], LDMX [120], PandaX-II [121], SENSEI [122], Oscura [123] etc. They have given an upper bound on the DM-e scattering cross-section, which can also describe the detection possibility of low-mass DM. The details of the scattering cross-section are given in A. In our simplified model, since we have chosen MFV-type couplings, the coupling of an electron with the mediator is proportional to the mass of the electron, so we will get a suppression in the cross-section. Hence, this channel will not be relevant in our phenomenological study.

The investigation of gamma-ray annihilation spectra in indirect detection (ID) places constraints on the dark matter annihilation cross-section rates into standard model particle pairs such as $b\bar{b}$, $\tau^+\tau^-$ etc. Collaborations such as Fermi-LAT [124, 125], High Energy Stereoscopic System (H.E.S.S) [126], and Cherenkov Telescope Array (CTA) [127] have contributed to establishing these bounds. More details on these bounds can be found at [56, 128].

5 Analysis and Results

Our simplified model impacts various observables associated with the FCNC and FCCC heavy flavour decays as well as W - and Z -pole observables. Furthermore, the model parameters can be constrained from BBN bounds and the condition of DM thermal equilibrium. It also contributes to the present relic density of the universe and can be constrained by the DD and ID bounds of the DM. This section aims to examine the constraints on the model parameters derived from the available data on these processes. Given the vast amount of data to analyze, which could complicate the analysis, separately, we will focus on inputs that provide weaker constraints on the model parameters. This approach allows us to discard less relevant data sets in the later stages of the analysis. We have separately studied the impact of the data on the semi-leptonic FCNC processes $B \rightarrow K^{(*)}\mu^+\mu^-$, $B_s \rightarrow \phi\mu^+\mu^-$. In addition, we have analyzed constraints from meson mixing amplitudes ΔM_d , ΔM_s , and rare decays such as $B_{(s)}^0 \rightarrow \mu^+\mu^-$ and $K_{L,S} \rightarrow \mu^+\mu^-$. Constraints from CHARM experiments and invisible decays of pseudoscalar mesons were also included in the analysis. Furthermore, we have evaluated the impact of FCCC processes, W - and Z -pole observables, and imposed BBN and thermal equilibrium conditions to establish lower bounds on the couplings. Dark matter constraints were analyzed separately and in conjunction with these other observables. We also will discuss the constraint from the CHARM experiment separately, as that constraint is important for our analysis.

In this analysis, we focus on the low-mass limit of the mediator S . The constraints on the model parameters are expected to depend strongly on the mediator mass M_S . As discussed, we study several processes where S is a virtual particle and some decays where S is produced on-shell. To analyze the phenomenology and constraints on the model parameters, we have divided the parameter space into two regions based on the mass of the spin-0 mediator:

- $M_S > 3$ GeV.
- $M_S \leq 3$ GeV.

Note that for $M_S \leq 3$ GeV, in our model, we will have a contribution to $B \rightarrow K^{(*)}S$ decays which is not possible for $M_S > 3$ GeV. Therefore, we constrain the parameters separately for $M_S \leq 3$ GeV and the data set includes the data on $\mathcal{B}(B \rightarrow K^{(*)}S)$. In comparison, for $M_S > 3$ GeV, we will drop the data related to $\mathcal{B}(B \rightarrow K^{(*)}S)$.

We have also divided our analysis into three parts. First, we show the constraints from flavour and electroweak observables. Next, we studied the constraints from DM analysis, considering relic density, direct detection limits, electron scattering bounds, and indirect detection constraints, which are detailed in the appendix. Finally, we will present the correlated parameter space by analyzing both the flavour and electroweak constraints and the dark sector constraints.

5.1 Constraints from Flavour and Electroweak Precision Observables

In the following sections, we will discuss the constraints on the new physics parameter space. This analysis incorporates the FCNC, FCCC, and EWPOs mentioned earlier, as

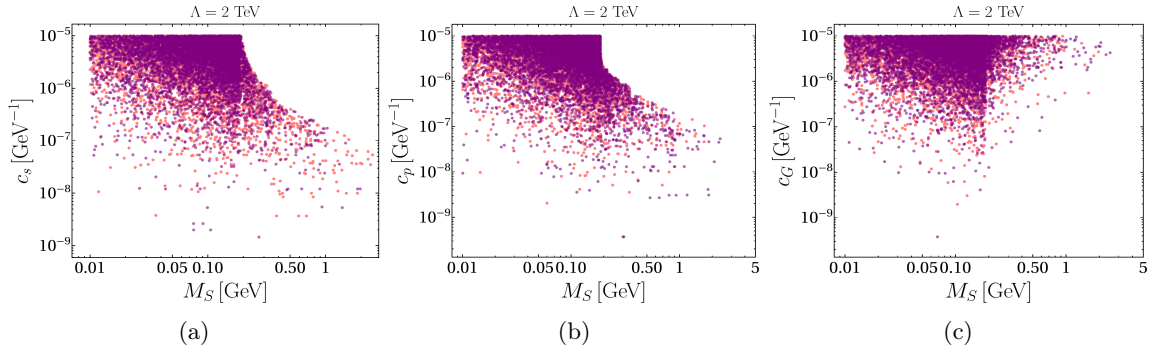


Figure 7. Excluded parameter space in mass-coupling ($c_i - M_S$) plane, from the constraint of CHARM of fix target experiment. In all these plots, we have varied c_s, c_p and c_G simultaneously. The pink points are related to the case where $M_\chi > M_S$ and for the purple points, we have taken $M_\chi = 1$ GeV with $c_{s(p)\chi} = 0.5$.

well as the constraints on the parameter space based on M_S , as discussed previously.

5.1.1 Bounds from Fixed Target Experiment

In Sec. 4.1.3, we have discussed the fixed target experiment where the spin-0 mediator S can be produced from meson decay, which further decays into pairs of electrons, muons, and photons. So far, no event(s) are detected in the CHARM detector [73], and the available upper bound is $N_{det} < 2.3$. We have used this bound as input in our analysis and obtained the plots in Fig. 7, which shows the excluded parameter space (colored regions) in the coupling-mass plane. The detailed theoretical expressions can be seen from the Sec. 4.1.3. While generating the plot, we kept all the parameters free except the cutoff scale, which was set at $\Lambda = 2$ TeV. As we can see from eq. (4.19), N_{det} depends on the total decay width of the mediator, so the mass and the coupling of DM will play a role here. For example, for a fixed value of the coupling N_{det} will decrease with the increasing values of M_S . The extreme left plot represents the variation of M_S with the scalar coupling c_s , and the middle and right plot is for the variation with c_p and c_G , respectively. We can see that the constraints on the couplings are more severe for $M_S \lesssim 0.2$ GeV. Conservatively, the allowed values of all the three couplings will $\lesssim 10^{-8}$ (in GeV^{-1}). We have checked that this data will not provide any strong correlations between the couplings c_s, c_p and c_G . Furthermore, the data from CHARM will not constrain the DM-mediator couplings $c_{s\chi}$ and $c_{p\chi}$, nor will it restrict the allowed region of M_χ . From the Fig. 7, we can see a dip region starting from $M_S \sim 2m_\mu$.

5.1.2 Bounds from Semileptonic $B(B_s) \rightarrow K^{(*)}(\phi) \ell^+ \ell^-$ Decays

We have taken into account the constraints obtained from the available data on the differential rates and angular observables in $B \rightarrow K^{(*)} \mu^+ \mu^-$ and $B_s \rightarrow \phi \mu^+ \mu^-$ decays. The NP contributions to these decays from our simplified model are discussed in the later part of the Sec. 4.1.2. Additionally, we have considered inputs on $R(K)$ and $R(K^*)$, as provided in

Λ [TeV]	M_S [GeV]	c_s [GeV $^{-1}$]	c_p [GeV $^{-1}$]	c_G [GeV $^{-1}$]
1	10	0.00078(3894)	-0.0167(45)	-0.00051(2651)
	5	0.00040(2106)	-0.0087(23)	-0.00024(1304)
	1	0.00023(2404)	-0.0050(14)	-0.00014(1428)
	0.1	0.00025(1888)	-0.0054(15)	-0.00015(1135)
2	10	0.089(33)	-0.0053(57)	-0.067(24)
	5	0.0397799(64)	-0.0023080(26)	-0.0300400(37)
	1	0.000099(12893)	-0.0039(13)	-0.000065(8617)
	0.1	-0.00021(2602)	0.0046(13)	0.00014(1713)

Table 2. Fit results of the couplings c_s , c_p and c_G from a fit to the available data on $B \rightarrow K^{(*)}\mu^+\mu^-$ and $B_s \rightarrow \phi\mu^+\mu^-$ decays and on $R_{K^{(*)}}$.

[66]. In this part of the analysis, we have not included the inputs on the branching fractions of the rare leptonic decays (eq. (4.11)).

As discussed earlier, the new physics contributions to these decays arise through the operators \mathcal{O}_s , \mathcal{O}'_s , \mathcal{O}_p , and \mathcal{O}'_p . We performed a χ^2 minimisation procedure using the *Mathematica*[®] package [129], incorporating the available data on differential rates, isospin asymmetry, and angular observables for the decays $B \rightarrow K\mu^+\mu^-$, $B \rightarrow K^*\mu^+\mu^-$, and $B_s \rightarrow \phi\mu^+\mu^-$. In this analysis, we focused solely on the muon sector, as the new physics effects in $b \rightarrow se^+e^-$ transitions are negligible. The relevant inputs for the differential rates and angular observables were obtained from several references [37–41, 63–65, 130, 131], and the fitting procedure follows the approach detailed in [90].

The fit results are shown in Table 2 for different values of the scalar mass M_S . Also, to note the dependence of the results with the cut-off scale Λ , we have done the fit for $\Lambda = 2, 1$ TeV, respectively. From the results, we note that the constraints from semi-leptonic $B \rightarrow K^{(*)}\mu^+\mu^-$ and $B_s \rightarrow \phi\mu^+\mu^-$ decays are relatively less stringent. Although a couple of data used in the fit are inconsistent with the respective SM predictions, the constraints on the NP parameters are very relaxed or practically unconstrained. This shows that the data on angular observables or the rates in these decays are not sensitive enough to the WCs $C_S^{(\prime)}$ and $C_P^{(\prime)}$ to put tight bounds. The allowed values of c_s , c_p and c_G could be of order 10^{-2} (in GeV $^{-1}$). Therefore, from now on, we will refer to the flavour observables, excluding these semi-leptonic $b \rightarrow s\ell\ell$ observables.

Observable	Value
$\mathcal{B}(B_s^0 \rightarrow \mu^+ \mu^-)$	$(3.09_{-0.43}^{+0.46} \quad {}_{-0.11}^{+0.15}) \times 10^{-9}$ [132]
$\mathcal{B}(B^0 \rightarrow \mu^+ \mu^-)$	$(0.12_{-0.07}^{+0.08} \pm 0.01) \times 10^{-9}$ [132]
V_L	0.995 ± 0.021 [59]
Δ_s	-0.0345 ± 0.0498 [58, 133]
Δ_d	-0.0497 ± 0.0518 [57, 58]
R_b	0.21629 ± 0.00066 [59]
R_c	0.1721 ± 0.0030 [59]
R_e	20.804 ± 0.050 [59]
R_μ	20.784 ± 0.034 [59]
R_τ	20.764 ± 0.045 [59]
A_e	0.1515 ± 0.0019 [59]
A_μ	0.142 ± 0.015 [59]
A_τ	0.143 ± 0.004 [59]
A_s	0.90 ± 0.09 [59]
A_c	0.670 ± 0.027 [59]
A_b	0.923 ± 0.020 [59]
$\delta(\Delta r) \times 10^3$	-0.191137 ± 0.691496 [134]

Table 3. List of few observables from FCNC, FCCC, and the Z-pole observables used in the scan.

5.1.3 Allowed Parameter Spaces from the Data on Flavour and EWPOs

In this section, we will present the results of the parameter space scan, incorporating all the important observables related to flavour and the electroweak precision test discussed earlier. In Table 3, we have summarised some of those observables. The full list of observables can be found from [56]. The latest update of the observable $\delta(\Delta r)$, is not included in our previous analysis as it came later. In addition, we have considered the branching fractions of a few rare invisible meson decays listed in Table 1 and a few rare decays of $B_{(s)}^0$ and K mesons. We have discussed all these observables in detail in the earlier sections. We will report results for two distinct mass ranges of M_S as outlined.

Mass region $M_S > 3$ GeV : This paragraph will show the allowed parameter spaces corresponding to $M_S > 3$. Actually, we will vary M_S in the region: $3 \text{ GeV} < M_S \leq 10 \text{ GeV}$. Here, we have taken all the constraints into account, which are mentioned in Table 3 along with the invisible decays like $P \rightarrow P' \chi \bar{\chi}$. As discussed, for $P \rightarrow P' \chi \bar{\chi}$ decay, S works as a virtual particle. So here, the mass of χ is allowed upto $M_\chi \leq \frac{M_P - M_{P'}}{2}$. Here, the constraint from CHARM will not be relevant. For the scan, we have varied the parameters within the

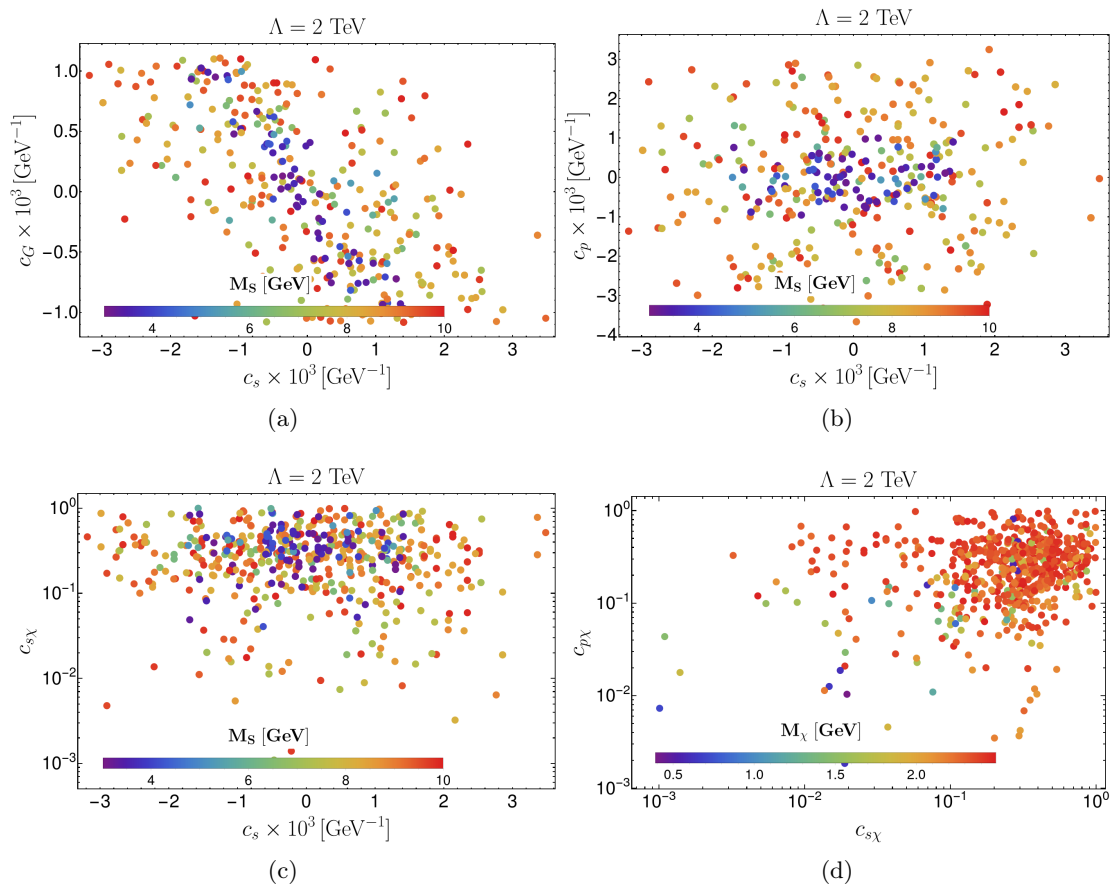


Figure 8. Correlation and parameter space of different couplings and mass allowed from all processes mentioned earlier, including invisible decays of mesons, when we are in $M_S > 3 \text{ GeV}$ region.

following ranges:

$$(|c_s|, |c_p|, |c_G|) \leq 0.1 \text{ GeV}^{-1} ; \quad 3 \text{ GeV} \leq M_S \leq 10 \text{ GeV} ; \quad c_{s(p)\chi} \leq 1 ; \quad M_\chi \leq 2.5 \text{ GeV}.$$

The plots in Fig. 8 show the allowed parameter space and the respective correlations in the coupling and mass planes. The allowed values of the parameters c_s and c_p can be up to $|c_{s(p)}| \leq 4 \times 10^{-3} \text{ GeV}^{-1}$, whereas, the allowed value of $|c_G| \leq 1.1 \times 10^{-3} \text{ GeV}^{-1}$. Also, we have got bounds on $c_{s(p)\chi}$ since the invisible decays will be sensitive to these couplings. As we can see, there are more concentrations of solutions for $c_{s(p)\chi} > 5 \times 10^{-2}$. These lower limits are due to the tight upper limits on $c_{s(p)}$. The correlation between $c_{s(p)}$ and $c_{s(p)\chi}$ comes from the branching ratios of the invisible decays, which vary as $\propto c_{s(p)}^2 c_{s(p)\chi}^2$, as shown in eq. (4.25). Furthermore, within the allowed ranges of the couplings, the dark matter mass M_χ prefers a region $\gtrsim 1.5 \text{ GeV}$, which we can see from Fig. 8d. Also, for smaller M_S , the allowed values of the couplings will be more constrained. For example, Fig. 8b shows that for $M_S \leq 5 \text{ GeV}$, the allowed values of $c_{s(p)}$ will be limited to the regions $|c_{s(p)}| \leq 0.001 \text{ GeV}^{-1}$, which also valid for c_G . For this mass region of the mediator, the tight constraints come from W -pole observable, rare decays of pseudoscalar mesons and the

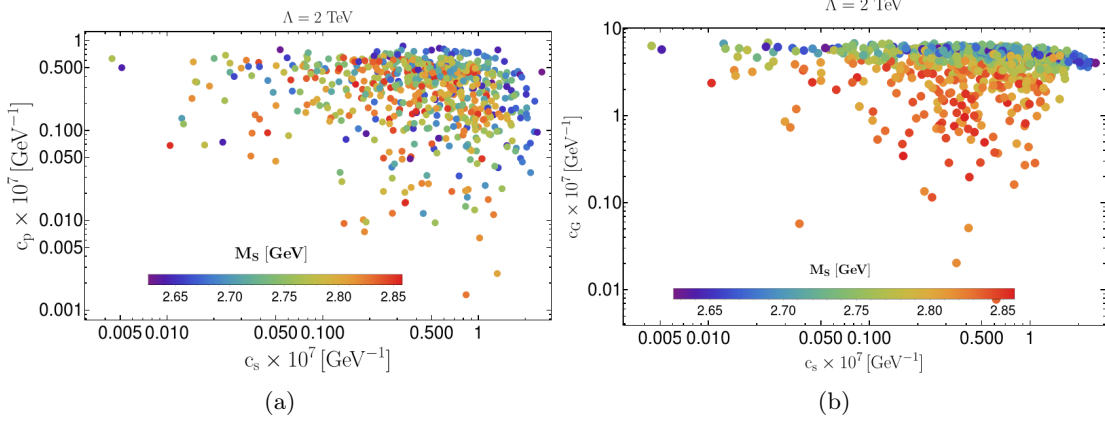


Figure 9. Correlation and parameter space of different couplings and mass allowed from all processes mentioned earlier including invisible decays of mesons for mediator mass range $M_S \leq (M_B - M_K)$, when we have allowed 1σ error in the observable of invisible decays of B meson.

invisible decays like $P \rightarrow P'\chi\bar{\chi}$, which is not the case for $M_S > 100$ GeV, for example, see [56].

Mass region $M_S \leq 3$ GeV : This paragraph shows the allowed parameter space of masses and couplings for $M_S \leq 3$ GeV. For the analysis, as inputs, we have taken all the flavour observables (FCNCs) and EWPOs, which we mentioned earlier. As mentioned, for these mass regions, the invisible decays like $P \rightarrow P'S$ with $P = B, K$ and $P' = K^{(*)}, \pi$ mesons will play an important role in constraining the parameter space. For the decay $B \rightarrow K^{(*)} + S$, we have taken the inputs from [54] where the variation of $\mathcal{B}(B \rightarrow K^{(*)} + S)$ with $M_S (\lesssim 3$ GeV) presented. For this process, we have analysed the distribution in branching ratios with M_S considering the errors at their 1σ and 2σ confidence interval. In addition, note that the $\mathcal{B}(B \rightarrow K + S)$ at its 1σ range is inconsistent with zero. However, at the 2σ range, this branching fraction is consistent with zero. On the other hand, the $\mathcal{B}(B \rightarrow K^* + S)$ is consistent with zero even within its 1σ error bar. Hence, the bounds on the parameters will depend on whether we are considering $\mathcal{B}(B \rightarrow K + S)$ at its 1σ or 2σ range. Here, since $\mathcal{B}(S \rightarrow \chi\bar{\chi}) \approx 1$, hence, we will not be able to constrain $c_{s\chi}$, $c_{p\chi}$ or M_χ using this data. Furthermore, constraints from fixed-target experiment (CHARM) will be effective in this region. As here $M_S \leq (M_P - M_{P'})$, we can get the invisible decay $P \rightarrow P'\chi\bar{\chi}$ via resonance i.e. $P \rightarrow P' + S$; $S \rightarrow \chi\bar{\chi}$. Hence, the constraint from the fix-target experiment is also taken into account.

In Fig. 9, we have shown the allowed parameter space in $c_s - c_p - c_G$ planes for $M_S \leq 3$ GeV for 1σ error band in the distribution in $\mathcal{B}(B \rightarrow K^{(*)} + S)$. The data from the fixed-target experiment and the $\mathcal{B}(B \rightarrow K^{(*)} + S)$ impose strong constraints on our parameter space. From the parameter scan, we get solutions only for $M_S \gtrsim 2.5$ GeV and the bounds are $(|c_s|, |c_p|, |c_G|) \lesssim 10^{-7} \text{ GeV}^{-1}$. The values of $M_S < 2.5$ GeV are not allowed since for these values, a simultaneous explanation of $\mathcal{B}(B \rightarrow K^{(*)} + S)$ and the bound from the fixed-target experiment is not possible. To satisfy the 1σ ranges of $\mathcal{B}(B \rightarrow K^{(*)} + S)$ we

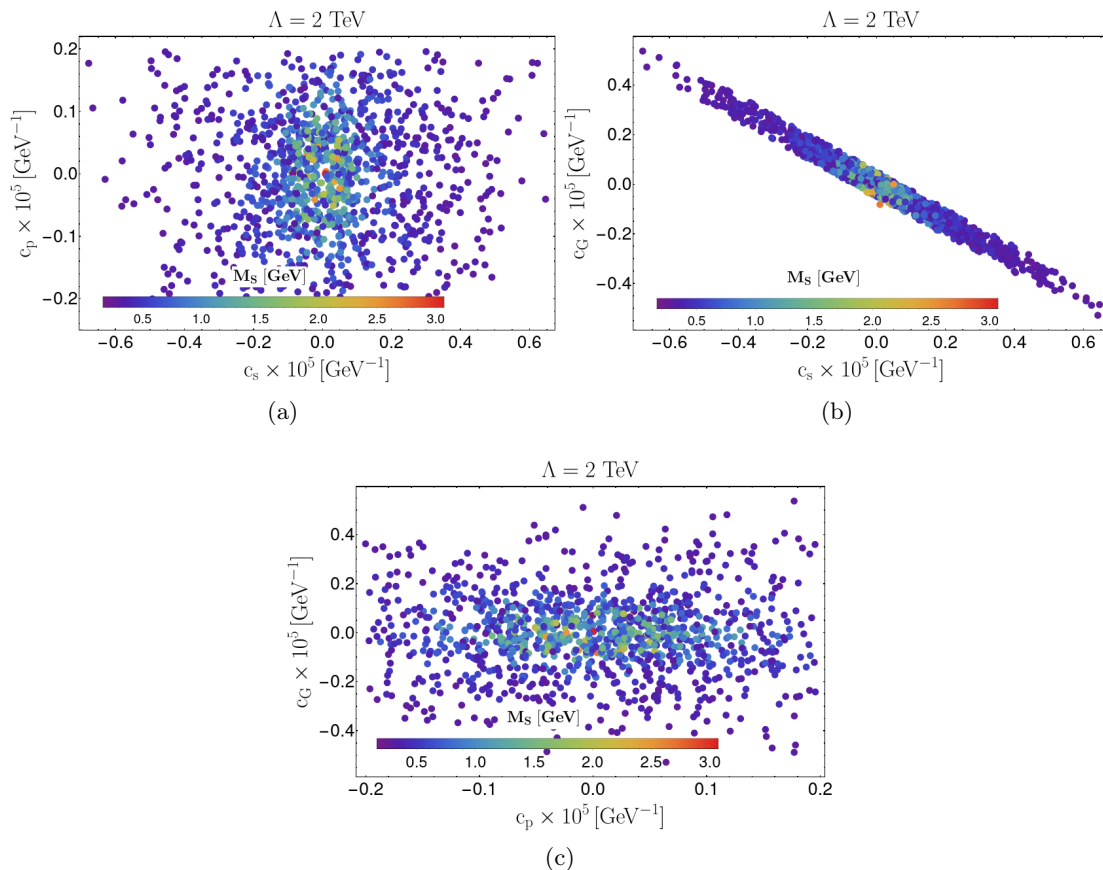


Figure 10. Correlation and parameter space of different couplings and mass allowed from all processes mentioned earlier including invisible decays of mesons for mediator mass range $M_S \leq 3$ GeV when we have allowed 2σ error in the observable of invisible decays of B meson.

need the values of the couplings to be in the range of order 10^{-9} to 10^{-7} (in GeV^{-1}) which is not allowed by the fixed-target experiment for $M_S < 2.5$ GeV (see Fig. 11). We get a very tight constraint than that of the previous case ($M_S > 3$ GeV) in all three coupling planes. The bounds on the couplings are as follows:

$$|c_s| \lesssim 3 \times 10^{-7} \text{GeV}^{-1}, \quad |c_p| \lesssim 10^{-7} \text{GeV}^{-1}, \quad |c_G| \lesssim 8 \times 10^{-7} \text{GeV}^{-1}. \quad (5.1)$$

Now, instead of 1σ , if we take 2σ bounds on $B \rightarrow K^{(*)} + S$, then there will be allowed parameter spaces for the whole region of $M_S \leq 3$ GeV. Also, the solutions are zero consistent since the 2σ bounds on $\mathcal{B}(B \rightarrow K^{(*)} + S)$ is zero consistent. We will only have an upper bound for this decay effectively. Even a very small value of the coupling can satisfy the bound. So, we get allowed space for the whole kinematical allowed region of M_S . The correlation among the parameters can be seen from Fig. 10. A strong correlation among the parameters c_s and c_G is obtained, and their magnitudes are positively correlated. Furthermore, the positive values of c_s prefer the negative values of c_G and vice-versa. The bounds we obtained for this case are:

$$|c_s| \lesssim 0.5 \times 10^{-5} \text{GeV}^{-1}; \quad |c_p| \lesssim 0.2 \times 10^{-5} \text{GeV}^{-1}; \quad |c_G| \lesssim 0.4 \times 10^{-5} \text{GeV}^{-1};$$

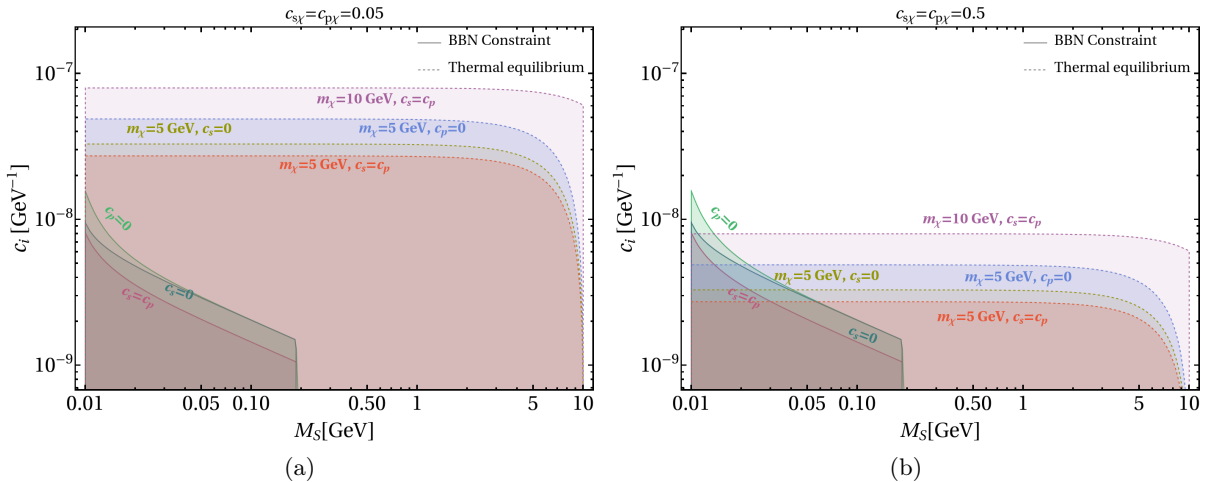


Figure 11. Excluded parameter space in mass-coupling ($c_i - M_S$) plane, from BBN constraint and condition for thermal equilibrium.

In the previous case ($M_S > 3$) GeV, we have seen that the bound gets relaxed with increasing the mass of the mediator. In this case ($M_S \leq 3$ GeV), the most stringent bound is obtained for a relatively higher mass of the mediator. This nature is coming from the CHARM constraint, which again can be realised from Fig. 7.

5.2 Cosmological Constraints

Since we are mainly interested in the low-mass region of the DM, the cosmological constraints will be important here to set a lower bound on the parameter space. Below, we will discuss BBN constraint and the condition of WIMP to be in thermal equilibrium.

BBN constraint and thermal equilibrium : As we have discussed in the previous section, if the lifetime of the spin-0 mediator $\tau_S > 1$ s, an important constraint from BBN will arise to bound the changes in entropy. To avoid this, we have taken the lifetime to be less than 1 s, which will give us a lower bound on the couplings c_s , c_p and c_G . We also have shown that these couplings cannot be very small for the DM to be in thermal equilibrium with the SM in order to satisfy the observed relic of the universe via the freeze-out method. In the low-mass region of the mediator, the coupling c_G won't be very relevant to us, for that matter, as being very low-mass, the mediator cannot decay to SM boson pairs. In this paragraph, we will discuss the bound on the coupling plane from the BBN constraint and the condition of thermal equilibrium.

Fig. 11 shows the excluded parameter space from both the constraint from BBN and thermal equilibrium discussed in Sec. 4.4. The boundary with solid lines shows the excluded regions from the BBN constraint. In our working model, the parameters c_s , c_p are the parameters which will be more sensitive to BBN constraints. Showing the variation with all these couplings is not possible in a single diagram, so we have plotted some coupling combinations. The dashed boundaries show the region where DM cannot be in thermal

equilibrium with SM. Here, the couplings of DM with the mediator will also play a role since we are studying the annihilation $\bar{\chi}\chi \rightarrow \bar{f}f$. To do the plot, we have fixed the couplings at $c_{s(p)\chi} = 0.5$ (right), and 0.05 (left). Increasing the couplings will increase $\langle\sigma v\rangle$, which will exclude the parameter space for less coupling (c_i) value. The parameter space will also depend on the mass of the DM M_χ . We have shown for two values of mass $M_\chi = 5$ GeV (blue, olive, red) and $M_\chi = 10$ GeV (violet). With increasing mass, the excluded region will be more. Also, for $M_\chi = 5$ GeV, we have plotted for purely scalar (blue), purely pseudoscalar (olive), and both equal (red) couplings.

The BBN constraint is coming from the lifetime of the spin-0 mediator S . The parameter c_G will be practically insensitive to cosmological constraints. The solid green region is for purely scalar coupling, teal is for purely pseudoscalar coupling, and pink is when both couplings are present and equal. Note that both the c_s and c_p are tightly constraints by BBN, and their numerical values $\lesssim 10^{-8}$ are not allowed for $M_S < 0.2$ GeV. However, the BBN constraints are relatively relaxed for $M_S > 0.2$ GeV, and important constraints will be from the thermal equilibrium. As mentioned, BBN constraint does not depend on the couplings $c_{s\chi}, c_{p\chi}$. On the other hand, the couplings $c_{s\chi}, c_{p\chi}$ are sensitive to the constraints of thermal equilibrium, which are also visible in the variations shown in Fig. 11. For small values of $c_{s(p)\chi}$, the allowed values for both couplings are $> 10^{-7} \text{ GeV}^{-1}$. Hence, for any value of the couplings and mass range, we are interested in the coupling region $c_{s,p} \gtrsim 10^{-7} \text{ GeV}^{-1}$, which is safe from these two constraints. So, in further analysis, where the couplings are $> 10^{-7} \text{ GeV}^{-1}$, we will not show these two constraints explicitly.

5.3 Combined analysis: Flavour + EWPOs + DM

In the previous sections, we have discussed separately the constraints we are getting from flavour and electroweak processes. The analysis by taking only the dark sector constraints into account describing DM phenomenology is given in appendix B, and the constraints are relatively relaxed. While performing the DM analysis, where only relic density and direct detection cross-section are taken into account, we have varied DM mass up to 10 GeV, as shown in the plots of Fig. 15 in the appendix.

In this section, we will find out the parameter spaces available to all the inputs, i.e., flavour and electroweak precision observables, as well as DM constraints. We provide the correlated parameter spaces, which are essential and relevant to many other phenomenological analyses. Following the discussions of the earlier sections, we have presented the results for two different mass regions.

In the region : $M_S > 3$ GeV

For the case when the mediator mass $M_S > 3$ GeV, the allowed parameter space and the correlations among the parameters are shown in the plots of Fig. 12. In order for the decays $P \rightarrow P'\chi\bar{\chi}$ to take place, the kinematic constrain on the DM mass M_χ will be: $M_\chi \leq \frac{M_P - M_{P'}}{2}$, as mentioned previously. Hence, we will only get allowed values of $M_\chi \lesssim 2.5$ GeV. Fig. 12a illustrates the parameter space in the $M_S - M_\chi$ plane with a variation of the coupling $c_{p\chi}$ (color variation). All the constraints allow a very limited region in the $M_S - M_\chi$ plane. Most of the allowed solutions prefer higher values of M_S (> 6 GeV).

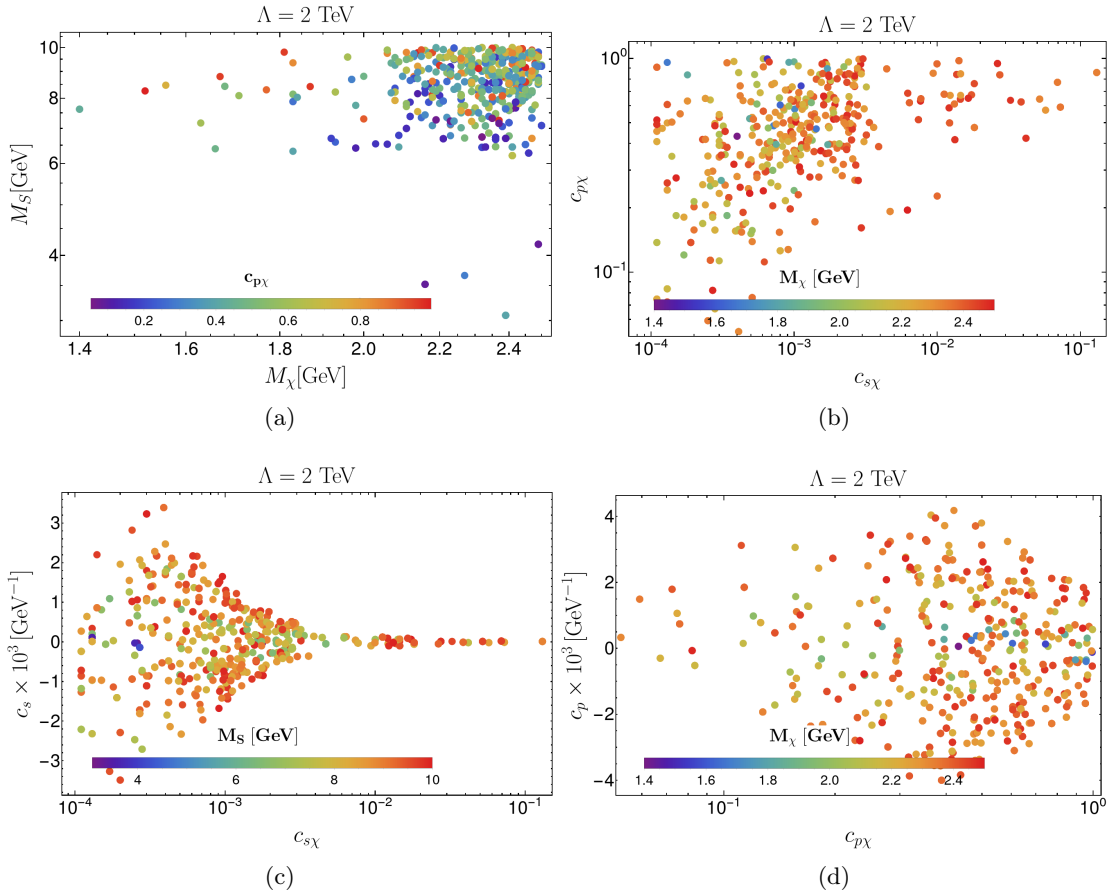


Figure 12. Correlations among the masses and the couplings allowed from all the flavor constraints as well as the DM constraints. Here $M_S > 3$ GeV.

Similarly, more concentrations of solutions are there for DM mass $M_\chi \gtrsim 2$ GeV. The points in the lower M_S, M_χ regions will be discarded in the combined analysis, which is otherwise allowed by the data on DM phenomenology; for example, see Fig. 15a in the appendix.

Fig. 12b displays the $c_{s\chi} - c_{p\chi}$ plane. Here, $c_{s\chi}$ is allowed upto $c_{s\chi} \lesssim 0.1$, constrained by the DM DD cross-section bound. Figs. 12c and 12d represent the correlations between $c_s, c_p, c_{s\chi}$ and $c_{p\chi}$ for the different allowed regions of M_S and M_χ . Note that the allowed values of c_s could be as large as $3 \times 10^{-3} \text{ GeV}^{-1}$ but for values of $c_{s\chi} \lesssim 0.001$. For $c_{s\chi} > 0.001$, the required values of c_s will be of order 10^{-4} GeV^{-1} or less. Also, for these values of $c_{s\chi}$ (> 0.001), the required values of $c_{p\chi}$ will be of order one or more. The allowed values of c_p could be as large as $4 \times 10^{-3} \text{ GeV}^{-1}$ and do not have a strong correlation with $c_{s(p)\chi}$ or with c_s . In our DM analysis, no constraints are derived for the couplings c_p and $c_{p\chi}$ since DD is independent of these couplings, and relic conditions are satisfied across the parameter space. However, in invisible decays, the branching ratio varies as $\propto c_p^2 c_{p\chi}^2$, necessitating lower c_p values for higher $c_{p\chi}$ to match experimental upper bounds.

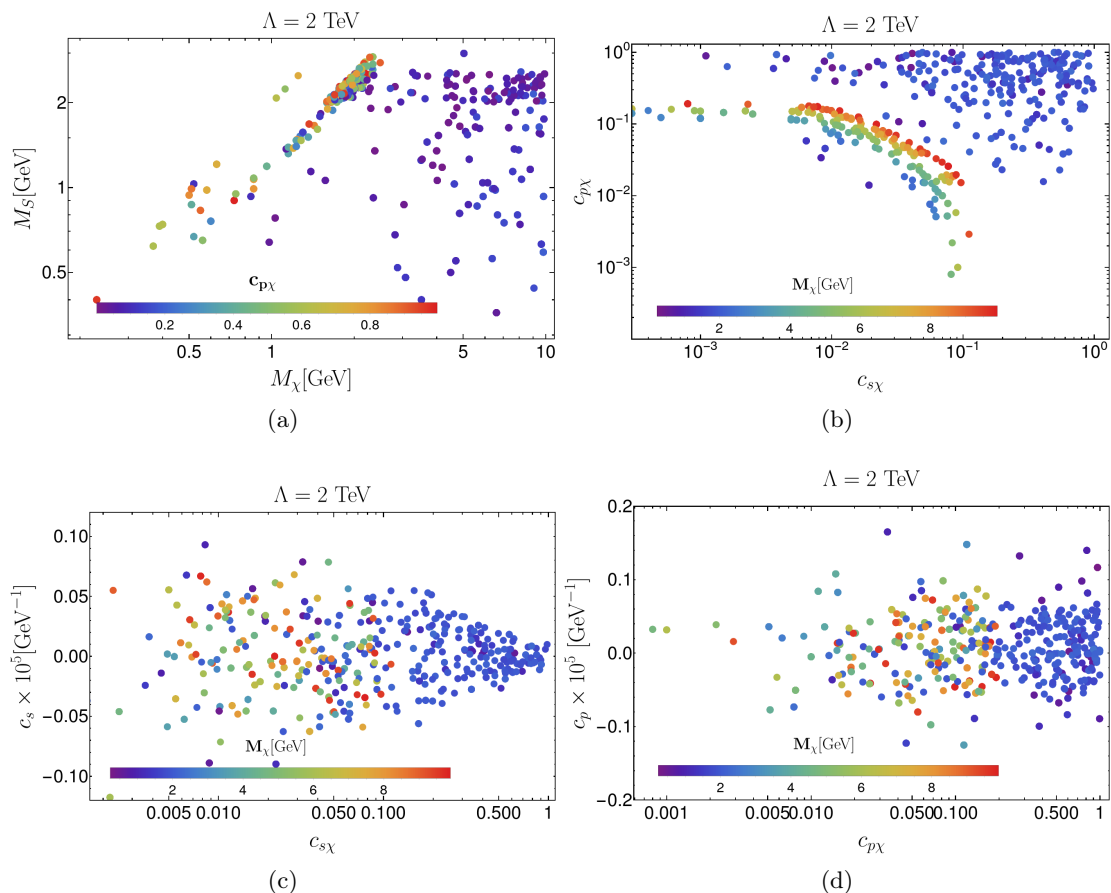


Figure 13. Correlations among the masses and the couplings allowed from all the flavour constraints (considering 2σ error of invisible decays) as well as the DM constraints, for the region $M_S \leq 3 \text{ GeV}$.

In the region : $M_S \leq 3 \text{ GeV}$

In the case where the mediator mass $M_S \leq 3 \text{ GeV}$, the parameter space is mostly constrained by the effects of invisible decays and fixed-target experiments. The parameter space allowed by flavour and electroweak processes is depicted in Fig. 10. In this subsection, we will explore how the DM constraints further modify the parameter space when combined with flavour constraints. While discussing the outcome from the analysis of only flavour and electroweak processes, we presented our results for two cases depending upon whether we take the 1σ error or 2σ error of the process $B \rightarrow K^{(*)}S$. For the case of 2σ error, the resulting interplay between the allowed parameter spaces is illustrated in the plots in Fig. 13.

As mentioned, the strongest constraint on this parameter space is coming from invisible decays ($P \rightarrow P' + S$) and fixed target experiment (CHARM). So, the constraint of flavour sector does not really depend on the mass of the DM (a small dependency is coming from the Breit-Wigner propagator of S). Similar to the previous case, here also we do not get any bound or impact of the coupling c_G from DM analysis. So to get the common parameter

space from flavour and DM, we have varied c_G in the range allowed from only flavour observables.

Fig. 13a shows the correlation between $M_S - M_\chi$, with color variation of the coupling $c_{p\chi}$. Since the flavour sector constraint does not have a noticeable dependency on the DM mass and the couplings, the whole M_χ region is allowed. However, we could see more concentration of allowed points for $M_\chi \gtrsim 1$ GeV and $M_S \gtrsim 1$ GeV. In figs. 13b, 13c and 13d we have shown the allowed solutions and the respective correlations for $c_{s(p)}$ and $c_{s(p)\chi}$ with the varying masses. Note that for values of $M_\chi \gtrsim 5$ GeV, the allowed solutions are concentrated around the values of $c_{p\chi}$ and $c_{s\chi}$ in the range 0.01 to 0.15. Values above these ranges are not allowed for $M_\chi \gtrsim 5$ GeV. Higher values of these couplings are allowed but for $M_\chi < 5$ GeV. For $c_{s\chi} < 0.1$, the allowed values of c_s could be as large as 1.5×10^{-6} GeV $^{-1}$. However, for $c_{s\chi} > 0.1$, we obtain $|c_s| \lesssim 0.5 \times 10^{-6}$ GeV $^{-1}$. The coupling c_p does not have noticeable correlations with the other parameters, and its values could be as large as 2×10^{-6} GeV $^{-1}$.

The plots in Fig. 13 illustrate the correlations among masses and couplings when considering a 2σ error for the invisible decays. If we instead take a 1σ error for the invisible decays of the B meson, the parameter space becomes more constrained Fig. 9 shows the allowed parameter space from only the flavour observables and EWPOs. A similar parameter space is obtained when combining dark sector constraints with these. The mediator mass is restricted to a very narrow region, as seen in Fig. 9. The mediator-SM couplings are allowed up to $|c_{s(p)}| \lesssim 10^{-7}$ GeV $^{-1}$. The correlations and allowed regions for $c_{s\chi} - c_{p\chi}$ remains unchanged. Since M_S is only allowed in the region $\approx (2.5 - 3.0)$ GeV, the allowed range for M_χ is also limited to $\gtrsim 2$ GeV, as can be seen from Fig. 13a.

6 Other Important Bounds

6.1 Bounds on Dimensionless Couplings

In our analysis, we have obtained bounds on the couplings c_s , c_p , and c_G , which can be expressed in terms of dimensionless couplings g_s , g_p , and g_V according to eqs. (2.2) and (2.4). In this section, we will discuss how the bounds on c_s , c_p , and c_G translate to dimensionless couplings g_s, g_p, g_V and the couplings of a toy model.

Bounds for $M_S > 3$ GeV: In our analysis, we get (in GeV $^{-1}$)

$$|c_s| \leq 4 \times 10^{-3}, \quad |c_p| \leq 4 \times 10^{-3}, \quad |c_G| \leq 1.1 \times 10^{-3}. \quad (6.1)$$

which will give us:

$$|g_s| \leq 0.70, \quad |g_p| \leq 0.70, \quad |g_V| \leq 0.27. \quad (6.2)$$

In connection with the DM phenomenology, the above bounds g_s will be applicable if we take the coupling $c_{s\chi} \lesssim 0.001$. For $c_{s\chi} > 0.001$ the bounds on g_s will be much stronger, like $|c_s| \leq 10^{-4}$ GeV $^{-1}$, which again gives us

$$|g_s| \leq 0.017. \quad (6.3)$$

Bounds for $M_S \leq 3 \text{ GeV}$: For this region of M_S , we get from our analysis (in GeV^{-1}):

$$|c_s| \leq 0.15 \times 10^{-5}, \quad |c_p| \leq 0.2 \times 10^{-5}, \quad |c_G| \leq 0.2 \times 10^{-5}, \quad (6.4)$$

which gives us the bounds on dimensionless couplings:

$$|g_s| \leq 2.6 \times 10^{-4}, \quad |g_p| \leq 3.5 \times 10^{-4}, \quad |g_V| \leq 5 \times 10^{-4}. \quad (6.5)$$

The above bound on g_s is applicable when $c_{s\chi} < 0.1$. For higher values, like $c_{s\chi} > 0.1$, the resulting bound on c_s will be smaller. Hence, the bound on $|g_s|$ will also be lesser, for example

$$|g_s| \leq 1 \times 10^{-4}. \quad (6.6)$$

6.2 Bounds on a Toy Model Parameters

The results of the above analysis are useful to constraint the couplings $\frac{C}{\Lambda}$ and $\frac{C'}{\Lambda}$ of the toy model with dimension five operators defined in eqs. (2.7) and (2.8), respectively. The couplings c_s , c_p and c_G are related to \mathbb{C}_s^S , \mathbb{C}_p^S and $\mathbb{C}_{W,Z}^S$ which are defined in eqs. (2.13) and (2.16), respectively. The parameter α is defined in eq. (2.11). The bounds on c_s , c_p and c_G will directly put constraints on $\frac{C}{\Lambda}$ and $\frac{C'}{\Lambda}$ alongside mixing angle θ and the VEV u . In this regard, also the data on the decay rate $\Gamma(h_1 \rightarrow f\bar{f})$ ($f = \text{SM fermions}$) are useful. The particle h_1 (in eq. (2.13)) represents the SM Higgs boson with a mass of $m_{h_1} = 125 \text{ GeV}$, while S is a BSM spin-0 particle. The Lagrangian shows that h_1 exhibits both scalar and pseudoscalar interactions, which can be constrained using data on Higgs decay widths to light quarks and leptons. The data on the branching ratios are available for the channels $h_1 \rightarrow (b\bar{b}, \mu^+\mu^-, \tau^+\tau^-)$, with upper limits on other possible decay channels [111, 135], which are given by

$$\mathcal{B}(h_1 \rightarrow b\bar{b}) = 0.53 \pm 0.08, \quad (6.7a)$$

$$\mathcal{B}(h_1 \rightarrow \tau^+\tau^-) = 0.060_{-0.007}^{+0.008}, \quad (6.7b)$$

$$\mathcal{B}(h_1 \rightarrow \mu^+\mu^-) = (2.6 \pm 1.3) \times 10^{-4}. \quad (6.7c)$$

We have analysed the data available on the Higgs decays separately and the respective correlations of $\frac{C}{\Lambda}$ with the VEV u and $\cos\theta$ are shown in the left plot in Fig. 14. Note that the solutions are allowed only in the regions when $\theta \rightarrow 0$ (or π), and for $u < 10 \text{ GeV}$, the allowed range of the coupling is given by

$$\left| \frac{C}{\Lambda} \right| < 5 \times 10^{-6} \text{ GeV}^{-1}. \quad (6.8)$$

For values of u around 100 GeV and above, the allowed solutions of $\left| \frac{C}{\Lambda} \right|$ will be of order 10^{-8} . On top of this, we can use the bounds on the c_s and c_p to constrain this coupling further. Note that the bounds c_s and c_p for $\mathbf{M_S} > \mathbf{3} \text{ GeV}$ is much more relaxed and will not restrict $\left| \frac{C}{\Lambda} \right|$ further than what we have obtained in eq. (6.8). However, the allowed solutions on c_s and c_p for $\mathbf{M_S} \leq \mathbf{3} \text{ GeV}$ will be relevant. The result of a combined analysis of the Higgs data and the bounds c_s and c_p is shown in the right plot in Fig. 14. The

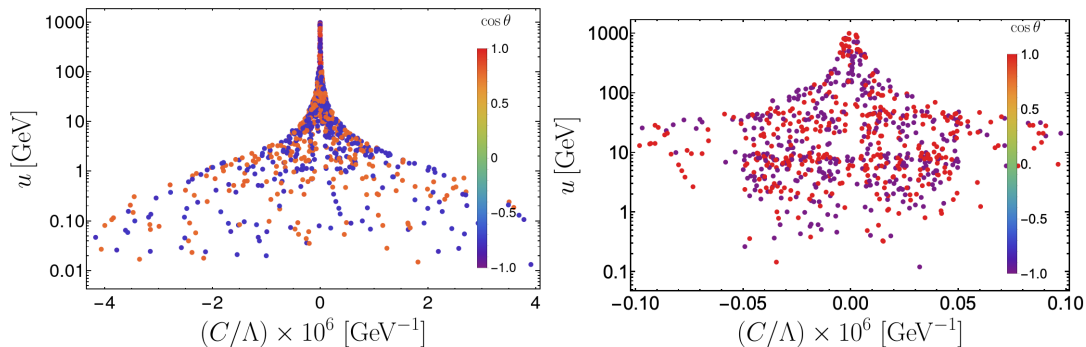


Figure 14. Allowed parameter space in the plane of $u - C/\Lambda$ (VEV of P -interaction strength), where the color variation is shown with the cosine of the mixing angle θ . The left plot is the allowed region for the case when we have taken only the Higgs data. The right plot shows the bound for the combined input of the Higgs decay data along with the bounds on c_s and c_p , which we get from our analysis.

allowed solutions will be one order of magnitude smaller than what we have shown in eq. (6.8).

The major constraints on $\frac{C'}{\Lambda}$ will mainly come from the bounds we obtain on c_G . Following which we have obtained for the case $M_S > 3$ GeV:

$$\left| \frac{C'}{\Lambda} \right| \leq 0.0022 \text{ GeV}^{-1}, \quad (6.9a)$$

and for $M_S \leq 3$ GeV, we get

$$\left| \frac{C'}{\Lambda} \right| \leq 0.4 \times 10^{-5} \text{ GeV}^{-1}. \quad (6.10a)$$

7 Summary

We have examined the allowed parameter spaces of a simplified dark matter model featuring fermionic dark matter and a spin-0 mediator that interacts with SM fermions and gauge bosons. This study focuses on the lower mass range of the spin-0 mediator i.e., $M_S \leq 10$ GeV. We divide the parameter space into two regions depending on the mass of the spin-0 mediator S ; one is $M_S > 3$ GeV, and the other one is $M_S \leq 3$ GeV, depending on whether the bounds of the invisible meson decays $P \rightarrow P'S$ can be used or not. We obtain bounds on the couplings strengths c_s , c_p and c_G associated with the interaction of the spin-0 mediator with the SM fermions and gauge bosons, respectively. We analyzed these two regions separately using all flavour and EWPOs. Then, we studied the constraints from the DM analysis. Finally, we identified a common parameter space that satisfies all available constraints, including the data on flavour, EWPOs, and DM constraints. The bounds on the couplings we are getting for the lower mass region ($M_S \leq 3$ GeV) are very tightly constrained. Also, we have obtained the lower bound on the couplings from the BBN and

the condition of DM to be in thermal equilibrium as χ is a WIMP-type DM. The BBN constraint is effective up to a very small mass. We get the lower limits on couplings $c_{s(p)}$ of the order of $\sim 10^{-8} \text{ GeV}^{-1}$ (strongly depends on mediator-DM couplings).

For $M_S > 3 \text{ GeV}$, the most stringent constraints are coming from rare decays and invisible decays of pseudoscalar mesons ($P \rightarrow P'\chi\bar{\chi}$). From only flavour and EWPOs we get, $|c_G| \lesssim 1.1 \times 10^{-3}$, $|c_{s(p)}| \lesssim 3 \times 10^{-3} \text{ GeV}^{-1}$. These bounds are stronger for smaller M_S . For $M_S \leq 5 \text{ GeV}$, we get ($|c_s|, |c_p|, |c_G|$) $\lesssim 5 \times 10^{-4} \text{ GeV}^{-1}$. Finally, we have scanned the parameter spaces and found correlations among the parameters allowed by the data related to DM phenomenology, flavour physics and EWPOs. The study suggests the concentration of solutions is only in the regions for $M_S > 6 \text{ GeV}$ and $1.75 < M_\chi \lesssim 2.50$ (in GeV). The region $M_S \leq 6 \text{ GeV}$ is disfavoured by the combined data on DM, flavour and EWPOs. The obtained bounds on $|c_G|$ and $|c_p|$ are as mentioned above (for $M_S > 5 \text{ GeV}$). However, the bounds on $|c_s|$ are highly correlated with $c_{s\chi}$, and the limit mentioned above will be applicable only when $c_{s\chi} < 0.001$. For $c_{s\chi} > 0.001$ the $|c_s|$ is tightly bound and could be of order 10^{-4} or less.

For $M_S \leq 3 \text{ GeV}$, the parameter space will mostly be constrained from invisible decay and fix-target experiment constraints. The most stringent bound for invisible decay comes from the decay $B \rightarrow KS$. The bounds on the couplings $|c_p|, |c_G|$ are $\lesssim 5 \times 10^{-6} \text{ GeV}^{-1}$. We observe similar limit on $|c_s|$ if we take $c_{s\chi} < 0.1$. For $c_{s\chi} \geq 0.1$, we get solutions only for $M_\chi \lesssim 3 \text{ GeV}$ and $|c_s| \lesssim 10^{-6} \text{ GeV}^{-1}$. For $M_\chi \geq 5 \text{ GeV}$, we get $(c_{p\chi}, c_{s\chi}) \lesssim 0.1$.

Using the bounds on $|c_s|, |c_p|, |c_G|$, we have obtained bounds on the dimensionless couplings $|g_s|, |g_p|$ and $|g_V|$, respectively. For $M_S > 3 \text{ GeV}$ the approximate bounds on $g_{s(p)}$ and g_V will be $\lesssim 0.7$ and $\lesssim 0.3$, respectively. For $M_S \lesssim 3 \text{ GeV}$ the respective approximate bounds are $g_{s/p/V} \lesssim 0.0004$ when we take the $|c_{s\chi}| < 0.001$. The allowed values of g_s will be less than 0.0001 when we consider $|c_{s\chi}| > 0.001$. These results suggest that the benchmark scenarios used in the collider analysis should be carefully chosen following the correlations among the parameters and their limits.

Finally, we have obtained bound on the couplings of the dimension-5 operators, which could lead to the type of interactions we are considering between the SM fermions or gauge bosons with the spin-0 mediator S . Since the mediator S mixes with the SM Higgs (h_1), the measured values on the branching fractions $h_1 \rightarrow f\bar{f}$ ($f = \text{fermions}$) will play an important role in the constraint of the mixing parameter ($\sin\theta$) and the other relevant couplings. We have obtained points that are allowed only for small mixing angles from a combined study of all the relevant inputs. In addition, we have obtained strong bounds on the couplings normalized by the scale of NP (Λ).

Appendix

A DM-electron cross-section

In the low-mass region of the DM, another significant direct detection process would be the DM-electron scattering cross-section. As mentioned in section 4.5, the bound and projected bound on the scattering cross-section is provided by various current and future experiments.

The amplitude square to calculate the scattering cross-section is given as follows:

$$|\mathcal{M}|^2 = \frac{m_e^2 (c_p^2 (-2m_e^2 - 2M_\chi^2 + s + t) + c_s^2 (2m_e^2 - 2M_\chi^2 + s + t)) \left((c_{p\chi}^2 + c_{s\chi}^2) (-2m_e^2 + s + t) + 2M_\chi^2 (c_{s\chi}^2 - c_{p\chi}^2) \right)}{(-2m_e^2 + M_S^2 - 2M_\chi^2 + s + t)^2}. \quad (\text{A.1})$$

The cross-section will be given by [112, 136]:

$$\sigma_{\chi e \rightarrow \chi e} = \frac{\mu_{\chi e}^2}{16\pi M_\chi^2 m_e^2} \overline{|\mathcal{M}_{\chi e}(q)|^2}_{q^2=\alpha^2 m_e^2}, \quad (\text{A.2})$$

where,

$$\overline{|\mathcal{M}_{\chi e}(q)|^2} = \overline{|\mathcal{M}_{\chi e}(q)|^2}_{q^2=\alpha^2 m_e^2} \times |F_{DM}(q)|^2 \quad (\text{A.3})$$

$\mu_{\chi e}$ is the reduced mass of DM and electron. $\overline{|\mathcal{M}_{\chi e}(q)|^2}$ is the squared matrix element averaged over the initial and summed over the final particle spin. The upper bound is provided on either the observable $\sigma_{\chi e \rightarrow \chi e} |F_{DM}(q)|^2$ or by taking $F_{DM}(q) = 1$.

B Allowed parameter spaces from the data on dark sector

In Sec. 5.1.3, we have studied the bounds on the parameter spaces coming from the study of all the flavour observables and the EWPOs. The bounds on the couplings c_s, c_p, c_G we get for the different values of M_S are very different. For $M_S > 3$ GeV, we get $c_{s,p} \approx 10^{-3}$ GeV $^{-1}$ and for $M_S \leq 3$ GeV, we get $c_{s,p} \approx 10^{-6}$ GeV $^{-1}$. So, to have a consistent analysis with those constraints, we will perform the DM analysis by dividing the parameter space in two regions: $M_S > 3$ GeV and $M_S \leq 3$ GeV. Since we are mainly interested in the portal couplings mediator with SM and DM, we have set the coupling $\lambda_1 = 0.001$ throughout our analysis.

For the region $M_S > 3$ GeV :

In this section, we will discuss the constraints on the parameter space for mediator mass $M_S > 3$ GeV. Fig. 15 shows the allowed parameter space. Here, we have taken relic density Ωh^2 and spin-independent direct detection cross-section bounds (mentioned earlier) into account.

Fig. 15, shows the allowed parameter space in mass and coupling plane. Here we have varied the parameters in the following regions:

$$(|c_s|, |c_p|) \leq 0.005 \text{ GeV}^{-1} ; \quad 3 \text{ GeV} \leq M_S \leq 10 \text{ GeV} ; \quad c_{s(p)\chi} \leq 1 ; \quad M_\chi \leq 10 \text{ GeV}. \quad (\text{B.1})$$

For $c_{s(p)\chi}$ the smallest division is 10^{-4} . As mentioned, mediator gauge boson coupling c_G will play no role here.

Fig. 15a, shows the allowed parameter space in $M_S - M_\chi$ plane. The color variation is shown for the DM pseudoscalar coupling $c_{p\chi}$. In the region $M_S \approx 2M_\chi$, we don't get many allowed points as they will be discarded after applying DD bounds. Also, for the region $M_\chi > M_S$, most points correspond to lower values of $c_{p\chi}$. Since, for $M_\chi > M_S$ region, the annihilation channel $\chi\bar{\chi} \rightarrow SS$ will open up. So, we need smaller values of DM couplings

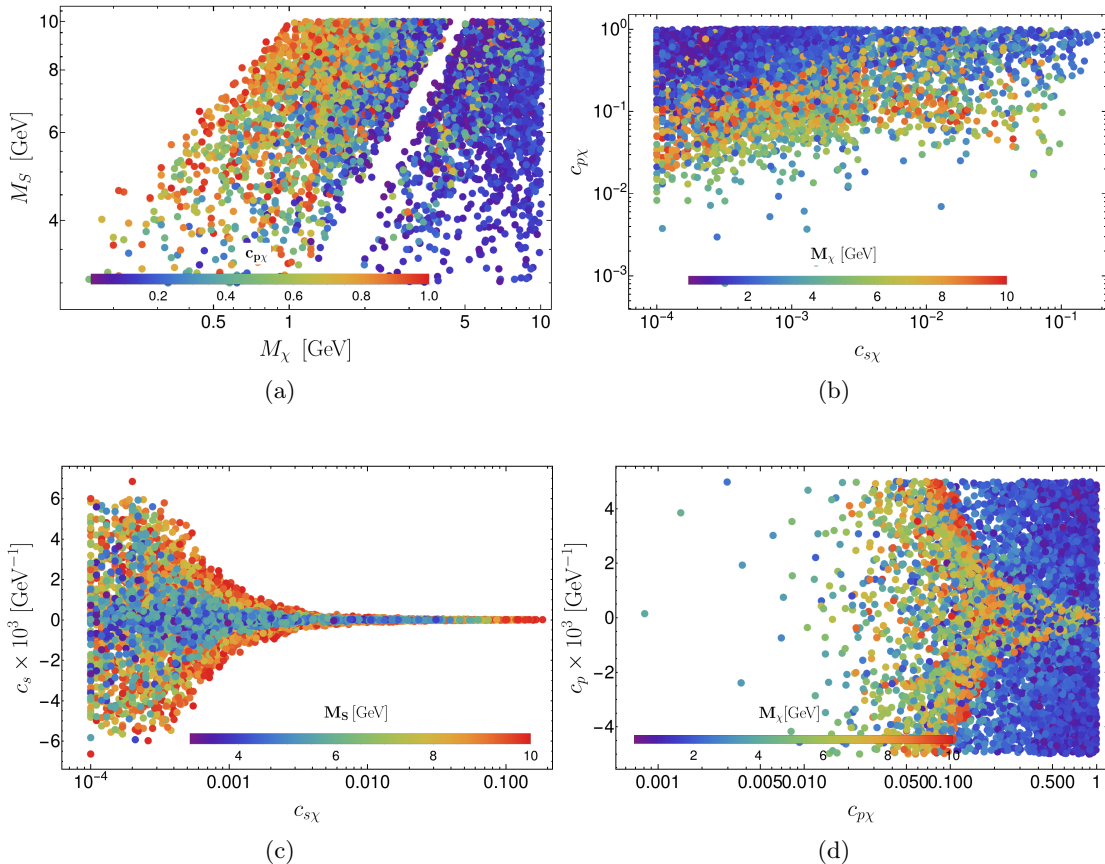


Figure 15. Correlations among the masses and the couplings allowed by DM relic density and the direct detection cross-section. Here, $M_S > 3$ GeV.

to satisfy the current relic. In that region, the points correspond to high $c_{p\chi}$ value and will have small values of c_s and c_p in order to satisfy the observed relic density.

Fig. 15b shows the correlation between the DM-mediator couplings $c_{s\chi} - c_{p\chi}$ plane. Here the color variation is shown with the DM mass M_χ . Here we are getting allowed value for $c_{s\chi}$ is up to $c_{s\chi} \lesssim 0.15$. $c_{s\chi}$ is highly constrained from DD bounds. We get a solution for all values of $c_{p\chi}$ up to 1. But for $M_\chi > 6$ GeV, both couplings gets constrained $c_{s(p)\chi} \leq 0.1$. Also, except for larger $c_{s\chi}$, very small values of c_s are needed to satisfy the bounds.

Similarly Fig. 15c shows the allowed parameter space in $c_s - c_{s\chi}$ plane. The correlation among them mainly comes from the DD bounds. The color variation is shown with the mediator mass M_S . The variation of DD cross-section with these three parameters can be seen from eq. (4.57). With increasing $c_{s\chi}$, smaller c_s is needed to satisfy the DD bound. For $c_{s\chi} \geq 0.005$, c_s will be bounded to $|c_s| \leq 0.0001$ GeV $^{-1}$. This bound will be further strict for the lower M_S and higher $c_{s\chi}$.

Lastly, the Fig. 15d shows the correlation among the pseudoscalar couplings $c_{p\chi} - c_p$ which comes from the relic density. We get solutions for the whole region of c_p varied. For higher mass of DM $M_\chi \geq 5$ GeV and $c_{p\chi} \geq 0.5$, c_p will be constrained as: $|c_p| \lesssim$

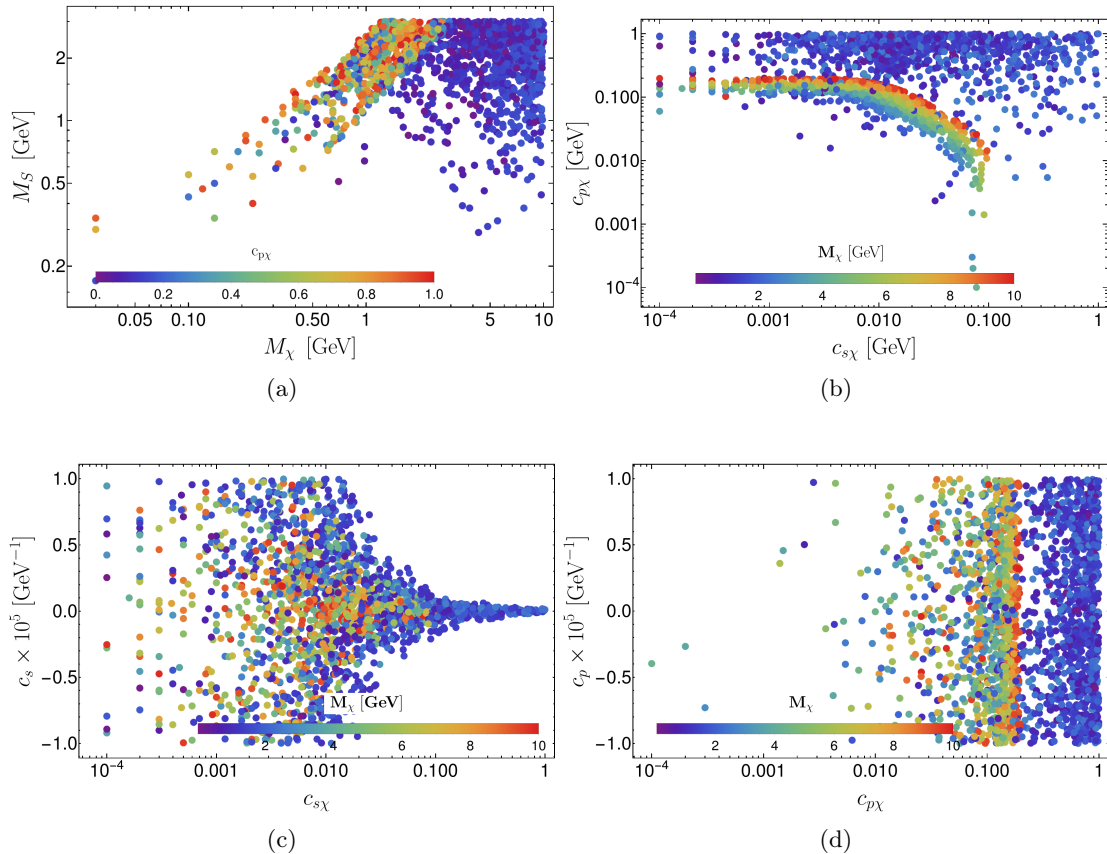


Figure 16. Correlations between masses and couplings allowed by the DM relic density and direct detection cross-section constraints, with $M_S \leq 3$ GeV.

$0.5 \times 10^{-3} \text{ GeV}^{-1}$.

In the mass region $M_S > 3$ GeV, the most of the parameter space is allowed except for c_s , which will be very constrained for larger $c_{s\chi}$. Also we get strong correlations among the masses as well as couplings, whose effect we can realise from the final combined parameter spaces.

For the region $M_S \leq 3$ GeV :

Here we will discuss DM phenomenology for $M_S \leq 3$ GeV. We have varied the couplings $c_{s,p}$ in the proximity of flavour allowed region. Here we have varied the parameters in the following range

$$(|c_s|, |c_p|) \leq 10^{-5} \text{ GeV}^{-1}; \quad 0.01 \text{ GeV} \leq M_S \leq 3 \text{ GeV}; \quad c_{s(p)\chi} \leq 1; \quad M_\chi \leq 10 \text{ GeV}. \quad (\text{B.2})$$

Similar to the previous case, here also we have taken relic and direct detection constraints into account.

Fig. 16 shows the correlations and bounds on parameter space from dark sector constraints for $M_S \leq 3$ GeV. Fig. 16a shows the correlation between DM mass and mediator

mass. The color variation is shown with the coupling $c_{p\chi}$. Most of the parameter space is satisfied for the smaller value of the coupling. Higher value of $c_{p\chi}$ is allowed for the regions: $M_\chi < M_S$. Large values of $c_{s\chi}$ is allowed in this region only. The region $M_\chi > 3$ GeV, is satisfied for lower values of $c_{s(p)\chi}$.

In Fig. 16b, the correlation between DM couplings $c_{s\chi}$ and $c_{p\chi}$ is shown. We can see two different regions in this plot. For higher values of DM mass, $M_\chi \gtrsim 3$ GeV, the couplings is restricted to $c_{s(p)\chi} \lesssim 0.1$. This region is the effect of the DM annihilation process $\chi\bar{\chi} \rightarrow SS$. Since we have both s and t-channel annihilation diagrams contributing to relic density, to get the observed relic density we need smaller $c_{s\chi}$ and $c_{p\chi}$. Also, since the cross-section mostly vary as: $\sigma_{\chi\bar{\chi} \rightarrow SS} \propto (c_{s\chi}^2 + c_{p\chi}^2)$, we get such circle type pattern. The region above the circle is for other annihilation channels except for SS . The higher values of coupling space can only be accessed by the lower mass of the DM.

Fig. 16c, the parameter space is shown in the plane $c_{s\chi} - c_s$, with M_χ in the color variation. The allowed value of c_s is very restricted for higher $c_{s\chi}$. (For $c_{p\chi}$ no such constraint is seen). This constraint is from only the DD cross-section, similar to the previous case. Also, for $M_\chi \geq 3$ GeV, the couplings is restricted to $|c_s| \leq 0.1$ GeV⁻¹. The region $c_{s\chi} \geq 0.1$ can only be accessed by smaller DM mass $M_\chi < 3$ GeV. The variation of these two couplings with M_S will be opposite that of M_χ , as the correlation with M_S is coming from the direct detection bound. For $c_\chi \geq 0.1$, we have $c_s \leq 10^{-6}$ GeV⁻¹. Also for this region $M_S \gtrsim 1.5$ GeV.

The Fig. 16d, shows the correlation among $c_p - c_{p\chi}$ with a color variation of the DM mass M_χ . As mentioned earlier, for higher DM mass, $c_{p\chi}$ will be constrained up to $c_{p\chi} \lesssim 0.1$, which can also be seen from here. We get the whole region of c_p as an allowed solution, as c_p cannot be constrained from the DD cross-section. No correlation with mediator mass M_S is seen from here as c_p and $c_{p\chi}$ do not contribute to the spin-independent direct detection cross-section.

We dont get much allowed parameter space corresponding to smaller M_χ , which can be seen for all the above plots. Plots in Fig. 16, shows the region with smaller M_χ needs smaller M_S to satisfy relic and direct detection constraints. The region of larger $c_{s(p)\chi}$ is only accessabke for smaller DM mass M_χ . This correlation will further constrain the parameter spaces when doing the combined analysis with all the constraints of flavour, EWPOs and DM.

References

- [1] Y. Bai and J. Berger, *Fermion Portal Dark Matter*, *JHEP* **11** (2013) 171 [[1308.0612](#)].
- [2] D. Schmeier, *Effective Models for Dark Matter at the International Linear Collider*, other thesis, 8, 2013, [[1308.4409](#)].
- [3] M.R. Buckley, D. Feld and D. Goncalves, *Scalar Simplified Models for Dark Matter*, *Phys. Rev. D* **91** (2015) 015017 [[1410.6497](#)].
- [4] J. Abdallah et al., *Simplified Models for Dark Matter and Missing Energy Searches at the LHC*, [1409.2893](#).

- [5] J. Abdallah et al., *Simplified Models for Dark Matter Searches at the LHC*, *Phys. Dark Univ.* **9-10** (2015) 8 [[1506.03116](#)].
- [6] A. Berlin, S. Gori, T. Lin and L.-T. Wang, *Pseudoscalar Portal Dark Matter*, *Phys. Rev. D* **92** (2015) 015005 [[1502.06000](#)].
- [7] S. Baek, P. Ko, M. Park, W.-I. Park and C. Yu, *Beyond the Dark matter effective field theory and a simplified model approach at colliders*, *Phys. Lett. B* **756** (2016) 289 [[1506.06556](#)].
- [8] C. Englert, M. McCullough and M. Spannowsky, *S-Channel Dark Matter Simplified Models and Unitarity*, *Phys. Dark Univ.* **14** (2016) 48 [[1604.07975](#)].
- [9] A. Albert et al., *Towards the next generation of simplified Dark Matter models*, *Phys. Dark Univ.* **16** (2017) 49 [[1607.06680](#)].
- [10] A. De Simone and T. Jacques, *Simplified models vs. effective field theory approaches in dark matter searches*, *Eur. Phys. J. C* **76** (2016) 367 [[1603.08002](#)].
- [11] G. Arcadi, M. Dutra, P. Ghosh, M. Lindner, Y. Mambrini, M. Pierre et al., *The waning of the WIMP? A review of models, searches, and constraints*, *Eur. Phys. J. C* **78** (2018) 203 [[1703.07364](#)].
- [12] M. Bauer, M. Klassen and V. Tenorth, *Universal properties of pseudoscalar mediators in dark matter extensions of 2HDMs*, *JHEP* **07** (2018) 107 [[1712.06597](#)].
- [13] G. Arcadi, M. Lindner, F.S. Queiroz, W. Rodejohann and S. Vogl, *Pseudoscalar Mediators: A WIMP model at the Neutrino Floor*, *JCAP* **03** (2018) 042 [[1711.02110](#)].
- [14] D. Abercrombie et al., *Dark Matter benchmark models for early LHC Run-2 Searches: Report of the ATLAS/CMS Dark Matter Forum*, *Phys. Dark Univ.* **27** (2020) 100371 [[1507.00966](#)].
- [15] LHC DARK MATTER WORKING GROUP collaboration, *LHC Dark Matter Working Group: Next-generation spin-0 dark matter models*, *Phys. Dark Univ.* **27** (2020) 100351 [[1810.09420](#)].
- [16] C. Arina, *Impact of cosmological and astrophysical constraints on dark matter simplified models*, *Front. Astron. Space Sci.* **5** (2018) 30 [[1805.04290](#)].
- [17] G. Arcadi, A. Djouadi and M. Raidal, *Dark Matter through the Higgs portal*, *Phys. Rept.* **842** (2020) 1 [[1903.03616](#)].
- [18] G. Arcadi, G. Busoni, T. Hugle and V.T. Tenorth, *Comparing 2HDM + Scalar and Pseudoscalar Simplified Models at LHC*, *JHEP* **06** (2020) 098 [[2001.10540](#)].
- [19] G. Arcadi, A. Djouadi and M. Kado, *The Higgs-portal for vector dark matter and the effective field theory approach: A reappraisal*, *Phys. Lett. B* **805** (2020) 135427 [[2001.10750](#)].
- [20] P. Cea, *Evidence of the true Higgs boson H_T at the LHC Run 2*, *Mod. Phys. Lett. A* **34** (2019) 1950137 [[1806.04529](#)].
- [21] F. Richard, *Evidences for a pseudo scalar resonance at 400 GeV Possible interpretations*, [2003.07112](#).
- [22] CMS collaboration, *Search for a standard model-like Higgs boson in the mass range between 70 and 110 GeV in the diphoton final state in proton-proton collisions at $\sqrt{s} = 8$ and 13 TeV*, *Phys. Lett. B* **793** (2019) 320 [[1811.08459](#)].

- [23] CMS collaboration, *Dark sector searches with the CMS experiment*, [2405.13778](#).
- [24] ATLAS collaboration, *Search for a new pseudoscalar decaying into a pair of muons in events with a top-quark pair at $s=13$ TeV with the ATLAS detector*, *Phys. Rev. D* **108** (2023) 092007 [[2304.14247](#)].
- [25] ATLAS, CMS collaboration, *Extra Higgs boson searches at the LHC*, in *12th International Workshop on the CKM Unitarity Triangle*, 4, 2024 [[2404.03571](#)].
- [26] L. Rygaard, J. Niedziela, R. Schäfer, S. Bruggisser, J. Alimena, S. Westhoff et al., *Top Secrets: long-lived ALPs in top production*, *JHEP* **10** (2023) 138 [[2306.08686](#)].
- [27] G. Hiller, *B physics signals of the lightest CP odd Higgs in the NMSSM at large $\tan\beta$* , *Phys. Rev. D* **70** (2004) 034018 [[hep-ph/0404220](#)].
- [28] M.J. Dolan, F. Kahlhoefer, C. McCabe and K. Schmidt-Hoberg, *A taste of dark matter: Flavour constraints on pseudoscalar mediators*, *JHEP* **03** (2015) 171 [[1412.5174](#)].
- [29] C. Arina, E. Del Nobile and P. Panci, *Dark Matter with Pseudoscalar-Mediated Interactions Explains the DAMA Signal and the Galactic Center Excess*, *Phys. Rev. Lett.* **114** (2015) 011301 [[1406.5542](#)].
- [30] E. Del Nobile, G.B. Gelmini, A. Georgescu and J.-H. Huh, *Reevaluation of spin-dependent WIMP-proton interactions as an explanation of the DAMA data*, *JCAP* **08** (2015) 046 [[1502.07682](#)].
- [31] D. Goncalves, P.A.N. Machado and J.M. No, *Simplified Models for Dark Matter Face their Consistent Completions*, *Phys. Rev. D* **95** (2017) 055027 [[1611.04593](#)].
- [32] K.-C. Yang, *Fermionic Dark Matter through a Light Pseudoscalar Portal: Hints from the DAMA Results*, *Phys. Rev. D* **94** (2016) 035028 [[1604.04979](#)].
- [33] S. Matsumoto, Y.-L.S. Tsai and P.-Y. Tseng, *Light Fermionic WIMP Dark Matter with Light Scalar Mediator*, *JHEP* **07** (2019) 050 [[1811.03292](#)].
- [34] Y.-T. Chen, S. Matsumoto, T.-P. Tang, Y.-L.S. Tsai and L. Wu, *Light thermal dark matter beyond p-wave annihilation in minimal Higgs portal model*, *JHEP* **05** (2024) 281 [[2403.02721](#)].
- [35] R. Bernabei et al., *The dark matter: DAMA/LIBRA and its perspectives*, in *16th Marcel Grossmann Meeting on Recent Developments in Theoretical and Experimental General Relativity, Astrophysics and Relativistic Field Theories*, 10, 2021, DOI [[2110.04734](#)].
- [36] T. Daylan, D.P. Finkbeiner, D. Hooper, T. Linden, S.K.N. Portillo, N.L. Rodd et al., *The characterization of the gamma-ray signal from the central Milky Way: A case for annihilating dark matter*, *Phys. Dark Univ.* **12** (2016) 1 [[1402.6703](#)].
- [37] LHCb collaboration, *Test of lepton universality using $B^+ \rightarrow K^+ \ell^+ \ell^-$ decays*, *Phys. Rev. Lett.* **113** (2014) 151601 [[1406.6482](#)].
- [38] LHCb collaboration, *Differential branching fractions and isospin asymmetries of $B \rightarrow K^{(*)} \mu^+ \mu^-$ decays*, *JHEP* **06** (2014) 133 [[1403.8044](#)].
- [39] LHCb collaboration, *Angular analysis of the $B^0 \rightarrow K^{*0} \mu^+ \mu^-$ decay using 3 fb^{-1} of integrated luminosity*, *JHEP* **02** (2016) 104 [[1512.04442](#)].
- [40] LHCb collaboration, *Angular Analysis of the $B^+ \rightarrow K^{*+} \mu^+ \mu^-$ Decay*, *Phys. Rev. Lett.* **126** (2021) 161802 [[2012.13241](#)].

- [41] BELLE collaboration, *Lepton-Flavor-Dependent Angular Analysis of $B \rightarrow K^* \ell^+ \ell^-$* , *Phys. Rev. Lett.* **118** (2017) 111801 [[1612.05014](#)].
- [42] A. Bharucha, D.M. Straub and R. Zwicky, *$B \rightarrow V \ell^+ \ell^-$ in the Standard Model from light-cone sum rules*, *JHEP* **08** (2016) 098 [[1503.05534](#)].
- [43] A. Biswas, S. Nandi, S.K. Patra and I. Ray, *New physics in $b \rightarrow s \ell \ell$ decays with complex Wilson coefficients*, *Nucl. Phys. B* **969** (2021) 115479 [[2004.14687](#)].
- [44] W. Altmannshofer, P. Ball, A. Bharucha, A.J. Buras, D.M. Straub and M. Wick, *Symmetries and Asymmetries of $B \rightarrow K^* \mu^+ \mu^-$ Decays in the Standard Model and Beyond*, *JHEP* **01** (2009) 019 [[0811.1214](#)].
- [45] LHCb collaboration, *Measurement of the $B_s^0 \rightarrow \mu^+ \mu^-$ decay properties and search for the $B^0 \rightarrow \mu^+ \mu^-$ and $B_s^0 \rightarrow \mu^+ \mu^- \gamma$ decays*, [2108.09283](#).
- [46] BELLE-II collaboration, *Evidence for $B^+ \rightarrow K^+ \nu \bar{\nu}$ Decays*, [2311.14647](#).
- [47] HPQCD collaboration, *Standard Model predictions for $B \rightarrow K \ell^+ \ell^-$, $B \rightarrow K \ell^+ \ell^+ \ell^-$ and $B \rightarrow K \nu \nu^-$ using form factors from $N_f=2+1+1$ lattice QCD*, *Phys. Rev. D* **107** (2023) 014511 [[2207.13371](#)].
- [48] E949, E787 collaboration, *Measurement of the $K^+ \rightarrow \pi^+ \nu \nu$ branching ratio*, *Phys. Rev. D* **77** (2008) 052003 [[0709.1000](#)].
- [49] BABAR collaboration, *Search for the Rare Decay $B \rightarrow K \nu \bar{\nu}$* , *Phys. Rev. D* **82** (2010) 112002 [[1009.1529](#)].
- [50] BELLE collaboration, *Search for $B \rightarrow h \nu \bar{\nu}$ decays with semileptonic tagging at Belle*, *Phys. Rev. D* **96** (2017) 091101 [[1702.03224](#)].
- [51] KOTO collaboration, *Study of the $K_L \rightarrow \pi^0 \nu \bar{\nu}$ Decay at the J-PARC KOTO Experiment*, *Phys. Rev. Lett.* **126** (2021) 121801 [[2012.07571](#)].
- [52] BABAR collaboration, *Search for $B \rightarrow K^{(*)} \nu \bar{\nu}$ and invisible quarkonium decays*, *Phys. Rev. D* **87** (2013) 112005 [[1303.7465](#)].
- [53] NA62 collaboration, *Measurement of the very rare $K^+ \rightarrow \pi^+ \nu \bar{\nu}$ decay*, *JHEP* **06** (2021) 093 [[2103.15389](#)].
- [54] W. Altmannshofer, A. Crivellin, H. Haigh, G. Inguglia and J. Martin Camalich, *Light new physics in $B \rightarrow K^{(*)} \nu \nu^-$* , *Phys. Rev. D* **109** (2024) 075008 [[2311.14629](#)].
- [55] U. Haisch and E. Re, *Simplified dark matter top-quark interactions at the LHC*, *JHEP* **06** (2015) 078 [[1503.00691](#)].
- [56] L. Kolay and S. Nandi, *Exploring Constraints on Simplified Dark Matter Model Through Flavour and Electroweak Observables*, [2403.20303](#).
- [57] HEAVY FLAVOR AVERAGING GROUP, HFLAV collaboration, *Averages of b -hadron, c -hadron, and τ -lepton properties as of 2021*, *Phys. Rev. D* **107** (2023) 052008 [[2206.07501](#)].
- [58] L. Di Luzio, M. Kirk, A. Lenz and T. Rauh, *ΔM_s theory precision confronts flavour anomalies*, *JHEP* **12** (2019) 009 [[1909.11087](#)].
- [59] PARTICLE DATA GROUP collaboration, *Review of Particle Physics*, *PTEP* **2022** (2022) 083C01.
- [60] LHCb collaboration, *Test of lepton universality in beauty-quark decays*, [2103.11769](#).

- [61] LHCb collaboration, *Constraints on the $K_S^0 \rightarrow \mu^+ \mu^-$ Branching Fraction*, *Phys. Rev. Lett.* **125** (2020) 231801 [[2001.10354](#)].
- [62] M. Beneke, C. Bobeth and R. Szafron, *Power-enhanced leading-logarithmic QED corrections to $B_q \rightarrow \mu^+ \mu^-$* , *JHEP* **10** (2019) 232 [[1908.07011](#)].
- [63] CDF collaboration, *Measurements of the Angular Distributions in the Decays $B \rightarrow K^{(*)} \mu^+ \mu^-$ at CDF*, *Phys. Rev. Lett.* **108** (2012) 081807 [[1108.0695](#)].
- [64] LHCb collaboration, *Measurement of the CP asymmetry in $B^+ \rightarrow K^+ \mu^+ \mu^-$ decays*, *Phys. Rev. Lett.* **111** (2013) 151801 [[1308.1340](#)].
- [65] CMS collaboration, *Measurement of angular parameters from the decay $B^0 \rightarrow K^{*0} \mu^+ \mu^-$ in proton-proton collisions at $\sqrt{s} = 8$ TeV*, *Phys. Lett. B* **781** (2018) 517 [[1710.02846](#)].
- [66] LHCb collaboration, *Test of lepton universality in $b \rightarrow s \ell^+ \ell^-$ decays*, *Phys. Rev. Lett.* **131** (2023) 051803 [[2212.09152](#)].
- [67] S. Bhattacharya, A. Biswas, S. Nandi and S.K. Patra, *Exhaustive model selection in $b \rightarrow s \ell \ell$ decays: Pitting cross-validation against the Akaike information criterion*, *Phys. Rev. D* **101** (2020) 055025 [[1908.04835](#)].
- [68] A.J. Buras, *Theoretical review of B physics*, *Nucl. Instrum. Meth. A* **368** (1995) 1 [[hep-ph/9509329](#)].
- [69] D. Becirevic, N. Kosnik, F. Mescia and E. Schneider, *Complementarity of the constraints on New Physics from $B_s \rightarrow \mu^+ \mu^-$ and from $B \rightarrow K l^+ l^-$ decays*, *Phys. Rev. D* **86** (2012) 034034 [[1205.5811](#)].
- [70] CHARM collaboration, *Search for Axion Like Particle Production in 400-GeV Proton - Copper Interactions*, *Phys. Lett. B* **157** (1985) 458.
- [71] J. Blumlein et al., *Limits on neutral light scalar and pseudoscalar particles in a proton beam dump experiment*, *Z. Phys. C* **51** (1991) 341.
- [72] M.E. Duffy et al., *Neutrino Production by 400-GeV/c Protons in a Beam-dump Experiment*, *Phys. Rev. D* **38** (1988) 2032.
- [73] J.D. Clarke, R. Foot and R.R. Volkas, *Phenomenology of a very light scalar ($100 \text{ MeV} < m_h < 10 \text{ GeV}$) mixing with the SM Higgs*, *JHEP* **02** (2014) 123 [[1310.8042](#)].
- [74] F. Bezrukov and D. Gorbunov, *Light inflaton Hunter's Guide*, *JHEP* **05** (2010) 010 [[0912.0390](#)].
- [75] D. Bečirević, G. Piazza and O. Sumensari, *Revisiting $B \rightarrow K^{(*)} \nu \bar{\nu}$ decays in the Standard Model and beyond*, *Eur. Phys. J. C* **83** (2023) 252 [[2301.06990](#)].
- [76] D.M. Straub, *flavio: a Python package for flavour and precision phenomenology in the Standard Model and beyond*, [1810.08132](#).
- [77] A.J. Buras, J. Harz and M.A. Mojahed, *Disentangling new physics in $K \rightarrow \pi \nu \nu$ and $B \rightarrow K(K^*) \nu \bar{\nu}$ observables*, [2405.06742](#).
- [78] KOTO collaboration, *Search for the $K_L \rightarrow \pi^0 \nu \bar{\nu}$ Decay at the J-PARC KOTO Experiment*, [2411.11237](#).
- [79] C. Bourrely, I. Caprini and L. Lellouch, *Model-independent description of $B \rightarrow \pi l \nu$ decays and a determination of $|V(ub)|$* , *Phys. Rev. D* **79** (2009) 013008 [[0807.2722](#)].

- [80] (HPQCD COLLABORATION)§, HPQCD collaboration, $B \rightarrow K$ and $D \rightarrow K$ form factors from fully relativistic lattice QCD, *Phys. Rev. D* **107** (2023) 014510 [2207.12468].
- [81] R.R. Horgan, Z. Liu, S. Meinel and M. Wingate, Lattice QCD calculation of form factors describing the rare decays $B \rightarrow K^* \ell^+ \ell^-$ and $B_s \rightarrow \phi \ell^+ \ell^-$, *Phys. Rev. D* **89** (2014) 094501 [1310.3722].
- [82] A. Biswas, S. Nandi, S.K. Patra and I. Ray, A closer look at the extraction of $|V_{ub}|$ from $B \rightarrow \pi \ell \nu$, *JHEP* **07** (2021) 082 [2103.01809].
- [83] N. Carrasco, P. Lami, V. Lubicz, L. Riggio, S. Simula and C. Tarantino, $K \rightarrow \pi$ semileptonic form factors with $N_f = 2 + 1 + 1$ twisted mass fermions, *Phys. Rev. D* **93** (2016) 114512 [1602.04113].
- [84] KOTO collaboration, Search for the $K_L \rightarrow \pi^0 \nu \bar{\nu}$ and $K_L \rightarrow \pi^0 X^0$ decays at the J-PARC KOTO experiment, *Phys. Rev. Lett.* **122** (2019) 021802 [1810.09655].
- [85] CLEO collaboration, Search for the familon via $B^{+-} \rightarrow \pi^{+-} X^0$, $B^{+-} \rightarrow K^{+-} X^0$, and $B^0 \rightarrow K^0(S) X^0$ decays, *Phys. Rev. Lett.* **87** (2001) 271801 [hep-ex/0106038].
- [86] CMS, ATLAS collaboration, Combination of the W boson polarization measurements in top quark decays using ATLAS and CMS data at $\sqrt{s} = 8$ TeV, *JHEP* **08** (2020) 051 [2005.03799].
- [87] CMS collaboration, Measurement of CKM matrix elements in single top quark t -channel production in proton-proton collisions at $\sqrt{s} = 13$ TeV, *Phys. Lett. B* **808** (2020) 135609 [2004.12181].
- [88] ATLAS collaboration, Measurement of the W boson polarisation in $t\bar{t}$ events from pp collisions at $\sqrt{s} = 8$ TeV in the lepton + jets channel with ATLAS, *Eur. Phys. J. C* **77** (2017) 264 [1612.02577].
- [89] CMS collaboration, Measurement of the W boson helicity fractions in the decays of top quark pairs to lepton + jets final states produced in pp collisions at $\sqrt{s} = 8$ TeV, *Phys. Lett. B* **762** (2016) 512 [1605.09047].
- [90] A. Biswas, L. Mukherjee, S. Nandi and S.K. Patra, Constraining new physics with possible dark matter signatures from a global CKM fit, *Phys. Rev. D* **107** (2023) 055041 [2111.01176].
- [91] LHCb collaboration, Measurement of the W boson mass, *JHEP* **01** (2022) 036 [2109.01113].
- [92] ATLAS collaboration, Improved W boson Mass Measurement using 7 TeV Proton-Proton Collisions with the ATLAS Detector, .
- [93] D0 collaboration, Measurement of the W Boson Mass with the D0 Detector, *Phys. Rev. Lett.* **108** (2012) 151804 [1203.0293].
- [94] CDF collaboration, High-precision measurement of the W boson mass with the CDF II detector, *Science* **376** (2022) 170.
- [95] J. Bernabeu, D. Comelli, A. Pich and A. Santamaria, Hard $m(t)$ corrections as a probe of the symmetry breaking sector, *Phys. Rev. Lett.* **78** (1997) 2902 [hep-ph/9612207].
- [96] J. Papavassiliou and A. Santamaria, Extra dimensions at the one loop level: $Z \rightarrow b$ anti- b and B anti- B mixing, *Phys. Rev. D* **63** (2001) 016002 [hep-ph/0008151].

- [97] A. Freitas, *Higher-order electroweak corrections to the partial widths and branching ratios of the Z boson*, *JHEP* **04** (2014) 070 [[1401.2447](#)].
- [98] G. Steigman, *Neutrinos And Big Bang Nucleosynthesis*, *Adv. High Energy Phys.* **2012** (2012) 268321 [[1208.0032](#)].
- [99] M. Kaplinghat, S. Tulin and H.-B. Yu, *Direct Detection Portals for Self-interacting Dark Matter*, *Phys. Rev. D* **89** (2014) 035009 [[1310.7945](#)].
- [100] PLANCK collaboration, *Planck 2018 results. VI. Cosmological parameters*, *Astron. Astrophys.* **641** (2020) A6 [[1807.06209](#)].
- [101] XENON collaboration, *First Dark Matter Search with Nuclear Recoils from the XENONnT Experiment*, *Phys. Rev. Lett.* **131** (2023) 041003 [[2303.14729](#)].
- [102] LZ collaboration, *First Dark Matter Search Results from the LUX-ZEPLIN (LZ) Experiment*, *Phys. Rev. Lett.* **131** (2023) 041002 [[2207.03764](#)].
- [103] PANDAX collaboration, *A search for dark matter-nucleon interactions with a dark mediator in PandaX-4T*, [2308.01540](#).
- [104] XENON collaboration, *First Search for Light Dark Matter in the Neutrino Fog with XENONnT*, [2409.17868](#).
- [105] DARKSIDE-50 collaboration, *Search for low-mass dark matter WIMPs with 12 ton-day exposure of DarkSide-50*, *Phys. Rev. D* **107** (2023) 063001 [[2207.11966](#)].
- [106] SENSEI collaboration, *First Direct-Detection Results on Sub-GeV Dark Matter Using the SENSEI Detector at SNOLAB*, *Phys. Rev. Lett.* **134** (2025) 011804 [[2312.13342](#)].
- [107] PANDAX collaboration, *Search for Dark-Matter–Nucleon Interactions with a Dark Mediator in PandaX-4T*, *Phys. Rev. Lett.* **131** (2023) 191002 [[2308.01540](#)].
- [108] LZ collaboration, *Search for new physics in low-energy electron recoils from the first LZ exposure*, *Phys. Rev. D* **108** (2023) 072006 [[2307.15753](#)].
- [109] SUPERCDMS collaboration, *Search for low-mass dark matter via bremsstrahlung radiation and the Migdal effect in SuperCDMS*, *Phys. Rev. D* **107** (2023) 112013 [[2302.09115](#)].
- [110] LUX collaboration, *Results of a Search for Sub-GeV Dark Matter Using 2013 LUX Data*, *Phys. Rev. Lett.* **122** (2019) 131301 [[1811.11241](#)].
- [111] PARTICLE DATA GROUP collaboration, *Review of particle physics*, *Phys. Rev. D* **110** (2024) 030001.
- [112] R. Essig, J. Mardon and T. Volansky, *Direct Detection of Sub-GeV Dark Matter*, *Phys. Rev. D* **85** (2012) 076007 [[1108.5383](#)].
- [113] R. Essig, T. Volansky and T.-T. Yu, *New Constraints and Prospects for sub-GeV Dark Matter Scattering off Electrons in Xenon*, *Phys. Rev. D* **96** (2017) 043017 [[1703.00910](#)].
- [114] XENON collaboration, *Low-mass dark matter search using ionization signals in XENON100*, *Phys. Rev. D* **94** (2016) 092001 [[1605.06262](#)].
- [115] CRESST collaboration, *First results from the CRESST-III low-mass dark matter program*, *Phys. Rev. D* **100** (2019) 102002 [[1904.00498](#)].
- [116] DAMIC-M collaboration, *First Constraints from DAMIC-M on Sub-GeV Dark-Matter Particles Interacting with Electrons*, *Phys. Rev. Lett.* **130** (2023) 171003 [[2302.02372](#)].

- [117] DARKSIDE collaboration, *Search for Dark Matter Particle Interactions with Electron Final States with DarkSide-50*, *Phys. Rev. Lett.* **130** (2023) 101002 [2207.11968].
- [118] J. Liao, Y. Gao, Z. Liang, Z. Ouyang, Z. Peng, L. Zhang et al., *Introduction to a low-mass dark matter project, ALETHEIA: A Liquid hELium Time projection cHambEr In dArk matter*, 2203.07901.
- [119] DARKSIDE-20K collaboration, *DarkSide-20k: A 20 tonne two-phase LAr TPC for direct dark matter detection at LNGS*, *Eur. Phys. J. Plus* **133** (2018) 131 [1707.08145].
- [120] LDMX collaboration, *Light Dark Matter eXperiment (LDMX)*, 1808.05219.
- [121] PANDAX-II collaboration, *Search for Light Dark Matter-Electron Scatterings in the PandaX-II Experiment*, *Phys. Rev. Lett.* **126** (2021) 211803 [2101.07479].
- [122] SENSEI collaboration, *SENSEI: Direct-Detection Results on sub-GeV Dark Matter from a New Skipper-CCD*, *Phys. Rev. Lett.* **125** (2020) 171802 [2004.11378].
- [123] OSCURA collaboration, *Skipper-CCD sensors for the Oscura experiment: requirements and preliminary tests*, *JINST* **18** (2023) P08016 [2304.04401].
- [124] FERMI-LAT collaboration, *Searching for Dark Matter Annihilation from Milky Way Dwarf Spheroidal Galaxies with Six Years of Fermi Large Area Telescope Data*, *Phys. Rev. Lett.* **115** (2015) 231301 [1503.02641].
- [125] FERMI-LAT collaboration, *Sensitivity Projections for Dark Matter Searches with the Fermi Large Area Telescope*, *Phys. Rept.* **636** (2016) 1 [1605.02016].
- [126] H.E.S.S. collaboration, *Search for dark matter annihilations towards the inner Galactic halo from 10 years of observations with H.E.S.S.*, *Phys. Rev. Lett.* **117** (2016) 111301 [1607.08142].
- [127] H. Silverwood, C. Weniger, P. Scott and G. Bertone, *A realistic assessment of the CTA sensitivity to dark matter annihilation*, *JCAP* **03** (2015) 055 [1408.4131].
- [128] S. Bhattacharya, L. Kolay and D. Pradhan, *Multiparticle scalar dark matter with \mathbb{Z}_N symmetry*, 2410.16275.
- [129] S.K. Patra, *OptEx*, 2019.
- [130] ATLAS collaboration, *Angular analysis of $B_d^0 \rightarrow K^* \mu^+ \mu^-$ decays in pp collisions at $\sqrt{s} = 8$ TeV with the ATLAS detector*, *JHEP* **10** (2018) 047 [1805.04000].
- [131] LHCb collaboration, *Branching Fraction Measurements of the Rare $B_s^0 \rightarrow \phi \mu^+ \mu^-$ and $B_s^0 \rightarrow f_2'(1525) \mu^+ \mu^-$ Decays*, *Phys. Rev. Lett.* **127** (2021) 151801 [2105.14007].
- [132] LHCb collaboration, *Analysis of Neutral B-Meson Decays into Two Muons*, *Phys. Rev. Lett.* **128** (2022) 041801 [2108.09284].
- [133] LHCb collaboration, *Precise determination of the $B_s^0 - \bar{B}_s^0$ oscillation frequency*, *Nature Phys.* **18** (2022) 1 [2104.04421].
- [134] CMS collaboration, *Measurement of the W boson mass in proton-proton collisions at $\sqrt{s} = 13$ TeV*, .
- [135] ATLAS collaboration, *A detailed map of Higgs boson interactions by the ATLAS experiment ten years after the discovery*, *Nature* **607** (2022) 52 [2207.00092].
- [136] J. Kopp, V. Niro, T. Schwetz and J. Zupan, *DAMA/LIBRA and leptonically interacting Dark Matter*, *Phys. Rev. D* **80** (2009) 083502 [0907.3159].